ORIGINAL RESEARCH ARTICLE

High-Speed Erichsen Testing of Grain-Refined 301LN Austenitic Stainless Steel Processed by Double-Reversion Annealing

ATEF HAMADA, ALI KHOSRAVIFARD, SUMIT GHOSH, MATIAS JASKARI, ANTTI JÄRVENPÄÄ, and PENTTI KARJALAINEN

Austenitic Cr–Ni stainless-type 301LN steel was subjected to a double-reversion annealing (DRA) treatment to develop bulk grain-refined microstructures. The tensile properties and formability of the DRA structures were determined by high-speed tensile and Erichsen cupping tests at a strain rate of 1.5 s^{-1} (50 mm s^{-1}) and compared with those of coarse-grained steel. Detailed microstructural features of the DRA structures were characterized using the electron backscatter diffraction technique and X-ray diffraction analysis. The DRA structures achieved by annealing for 1 second at 800 °C and 900 °C exhibited a superior combination of yield (~ 950 and 770 MPa, respectively) and tensile (~ 1050 and 950 MPa, respectively) strengths and ductility (~ 35 and 40 pct, respectively, as well as reasonable Erichsen index values under high-speed biaxial strain. Due to adiabatic heating, the DRA structures had higher austenite stability during high-speed stretch forming, *i.e.*, were less prone to strain-induced martensitic transformation. The finite-element method (FEM) was used to conduct coupled field thermomechanical analyses of the high-speed deformation processes for the coarse-grained and DRA structures. Comparison of the FEM analyses with the experimental results revealed a considerable influence (~ 20 pct) of martensitic transformation on the adiabatic temperature rise. The balance of the yield strength and Erichsen index value of the developed nanograined microstructure is comparable to that of coarse-grained commercial steel.

https://doi.org/10.1007/s11661-022-06659-5

I. INTRODUCTION

THE demand for high-strength with good ductility, formability, fatigue resistance, and corrosion resistance is continuously increasing, and steel products with enhanced performance are used in several applications. Their high strength makes them suitable candidates for lightweight structures with reduced costs.[1] Austenitic stainless steel is highly regarded due to its formability and corrosion resistance, which makes it a popular choice for several structural applications. However, despite its excellent corrosion resistance and good formability, the application of austenitic stainless steels is often still limited in the sheet-forming industry for the fabrication of automotive and aerospace structural components due to their low yield strength (~ 250 to 350 MPa).[2] Austenitic 17 pct Cr–7 pct Ni stainless steel (Type 301/301LN) is metastable due to its low stacking fault energy (SFE ≤ 15 mJ m^{-2}) and tends to undergo martensitic phase transformation during static/dynamic deformation.[3–7] Consequently, different techniques have been employed to promote grain refinement in this steel by utilizing the martensitic transformation upon heavy cold deformation followed by reversion annealing.[8] During the past two decades, reversion treatment has been established as an efficient route to fabricate submicron ultrafine grain (UFG) or even nanograined (NG) structures in metastable austenitic stainless steels.[9–16] Moallemi *et al.*[17] applied the reversion treatment to AISI 201 stainless steel at a range of temperatures (750 °C to 900 °C) and various times (15 to 1200 seconds) after heavy cold-rolling deformation of 90 pct to promote a nano/ultra-fine-grained structure. Abdi *et al.*[18] obtained a fine-grained structure of AISI 309Si stainless steel with an average grain size of ~ 11 μm after heavy cold

ATEF HAMADA, MATIAS JASKARI, and ANTTI JÄRVENPÄÄ are with the Kerttu Saalasti Institute, Future Manufacturing Technologies (FMT), University of Oulu, Pajatie 5, 85500 Nivala, Finland. Contact e-mail: atef.hamadasaleh@oulu.fi ALI KHOSRAVIFARD is with the Department of Advanced Calculations, Chemical, Petroleum & Polymer Engineering Research Center, Shiraz Branch, Islamic Azad University, Box 71993-1, Shiraz, Iran. SUMIT GHOSH and PENTTI KARJALAINEN are with the Materials and Mechanical Engineering, Centre for Advanced Steels Research, University of Oulu, P.O. Box 4200, 90014 Oulu, Finland.
Manuscript submitted December 8, 2021; accepted March 12, 2022.
Article published online March 31, 2022

deformation and subsequent reversion annealing at 1000 °C for 1 hour.

Recently, a new approach was employed to fabricate bulk materials with nanograined/ultrafine-grained structures. Chatterjee[19] applied multiple rolling deformations to 301LN at a warm-rolling temperature of 200 °C and cold rolling with consecutive annealing treatments at 700 °C for 20 minutes. These deformation and annealing cycles enhanced the fine-grained austenitic structure of 301LN with an average grain size of 4 μm.

Collectively speaking, this repetitive approach of cold rolling and annealing was applied to different materials to process a bulk nanostructured structure, *e.g.*, Ni, Ti, and Zr,[20] AZ31 magnesium alloy.[21] Hwang *et al.*[22] applied 4 cycles of repeated cold-rolling deformation to high-Mn TWIP steel (22Mn–0.6C wt pct). A subsequent intermediate annealing cycle between each cold-rolling deformation cycle was carried out at 600 °C for 600 seconds to achieve a grain structure of 2.0 μm.

In the same context, medium-Mn steel (Fe–0.11C–2.46Si–11.5Mn–0.38Al–0.029N) with a nanocrystalline structure was processed by repeated deformation and annealing. The nanograined structure of the studied steel promoted significant yield and tensile strengths of 790 MPa and a total elongation of 28 pct.[23] Fadhalah and Aleem[24] applied two different schemes of repetitive thermomechanical processing to 304 stainless steel by applying tensile strains of 0.4 for four cycles and 0.6 for two cycles at − 100 °C with deformation followed by annealing at 800 °C for 5 minutes. The two-cycle process in which a higher deformation strain of 0.6 was applied was more effective in inducing a finer grain structure with a grain size of 1.03 μm.

As recently reviewed,[8,25] a very large number of studies have been performed on Cr–Ni 301 and 301LN steels to improve their tensile properties by grain refinement with reversion treatment, and these studies include works by Somani *et al.*[26–28] and Järvenpää *et al.*[29–31] The grain refinement of metastable austenitic stainless steels shows marked effects on properties other than strength, such as fatigue, wear, and corrosion. Järvenpää *et al.*[32] found a significant improvement in the fatigue strength of UFG 301LN steel. Similarly, Hamada *et al.*[33,34] found that 301LN with a grain size of ~ 0.75 μm, produced by reversion annealing, showed improved fatigue resistance by 77 pct compared with the corresponding coarse-grained (CG) structure. Liu *et al.*[35] reported the increased wear resistance of metastable Cr–Ni steel. In addition, a uniform UFG structure exhibited simultaneous enhancement in mechanical strength and corrosion resistance.[36,37] Other potential uses of UFG austenitic stainless steels include biomedical applications.[38,39]

In the studies of Somani *et al.*,[26–28] Järvenpää *et al.*,[29–32] and Hamada *et al.*,[12,33,34] annealing was conducted using resistance heating in a Gleeble simulator, where high heating rates, strict temperature control, and short holding times from zero seconds were readily achieved. Hamada *et al.*[40] promoted grain refinement after heavy cold deformation by laser heating. Droste *et al.*[41] employed laser heating for the reversion treatment of 17Cr–7Ni–7Mn steel to produce a grain size of 3 to 8 μm. However, reversion processing by laser energy is not favorable for producing bulk material since the effective laser spot diameter, related to the heat-affected zone, is very small. Thus, induction heating has obvious advantages in this respect.

In general, austenitic stainless steels have good formability. However, the balance between the stretch formability and the mechanical strength of these materials is controlled by their grain structure.[42] Currently, our research group at the University of Oulu is focusing on enhancing the formability properties of reversion-treated steels. In a recent study, mechanical strength was promoted by double-reversion annealing (DRA).[43] DRA is a processing technique used to manufacture grain-refined materials by applying two-stage cold rolling and subsequent fast-heating annealing treatments. In the process, induction heating can be used for bulk products, but to more precisely control the processing variables, induction heating in the first stage and Gleeble resistance heating in the latter stage, as in the present work, only laboratory samples for experiments can be manufactured with this route. From previous work, a long-term process of repeated cold rolling with prolonged annealing treatments at low temperatures and durations of hours is applied to obtain ultrafine-grained structures at the micro/nanoscale. Interestingly, the advantage of our technique (DRA) is employing fast induction heating (~200 °C s^{-1}) at higher temperatures with very short-duration annealing (0.1 to 1 second). Furthermore, the DRA process makes it possible to apply heavy deformation reduction after each cycle, thereby, enhancing grain refinement. Economically, this new approach is desirable in the industry because it increases the cost efficiency of manufacturing bulk materials with grain-refined structures.

High-speed formability is a recent trend in sheet metal forming since it offers certain advantages, such as high productivity, high tool flexibility, and reduced component weight.[44,45] To the best of the authors' knowledge, the high-speed forming of reversion-refined grain structures of AISI 301/301LN stainless steels has not been reported in the literature. In the present research, the relation between the grain-refined structures of 301LN, achieved by DRA processing, and high-speed tensile and forming properties are studied. A finite-element modeling (FEM) was conducted to evaluate the adiabatic heating and deformation capacity of the different structures. The results were compared with those of CG commercial 301LN steel.

II. MATERIALS AND METHODS

A metastable austenitic stainless steel of grade AISI 301LN was obtained from Outokumpu Stainless Oy, Tornio Works (Tornio, Finland) in the form of 8-mm-thick hot-rolled sheets. The chemical composition was as follows: Fe–0.019C–1.15Mn–17.5Cr–6.5Ni–0.57-Si–0.14N (wt pct). The steel sheets were subjected to double-stage cold-rolling deformation at room temperature using a laboratory rolling mill. In the first stage,

the thickness reduction was 55 pct, *i.e.*, true strain ~ 0.7. Subsequently, reversion annealing treatment was conducted at 690 °C for 60 s using a pilot continuous induction heating (CIH) line with a 600-kW power unit. The reversion-annealed sheets were again cold rolled to 65 pct reduction at room temperature, *i.e.*, true strain ~ 1. Finally, the deformed material was subjected to additional reversion annealing treatments at different temperatures and times, 750 °C for 0.1 second, 800 °C for 1 second, and 900 °C for 1 second, followed by cooling by blowing air to room temperature. The second reversion treatment was conducted using a Gleeble 3800 thermomechanical simulator. Details of the DRA experiments are illustrated in Figure 1. The created structures are denoted according to the temperature and time of the second reversion annealing treatment, *e.g.*, DRA T750-0.1, DRA T800-1, and DRA T900-1.

Detailed microstructures of the DRA specimens were characterized by electron backscatter diffraction (EBSD) using field-emission scanning electron microscopy (FE-SEM; Zeiss Ultra Plus). EBSD mapping was conducted at an accelerating voltage of 15 kV with a step size of 0.01 μm. The average grain size of the different DRA structures was analyzed using the acquired grain structure EBSD maps based on measuring the areas of the grains by the elliptical fitting for each grain. These maps were processed by the grain reconstruction method using HKL-CHANNEL 5 software (Oxford Instruments, UK) to obtained detailed statistical information on the grain size distribution.

Furthermore, the DRA microstructures were characterized by transmission electron microscopy (TEM, Model) at 200 kV. The TEM investigations were conducted in bright field, diffraction pattern, and scanning transmission electron microscopy (STEM) mode. Thin wafers of thickness ~ 100 μm were extracted from the DRA specimens and thinned for TEM studies by a Struers TenuPol twinjet electropolisher system at a voltage of 30 V and a temperature of—25 °C in a solution of 10 vol pct perchloric acid.

X-ray diffraction (XRD) measurements (Rigaku Smart Lab 9kW) were carried out to estimate the average phase fractions of austenite and martensite. The scan speed was 7.2° min^{-1}, and data were obtained for 2θ angles of 45 to 130 deg using CoKα radiation. PDXL2 software was used to analyze the phase fractions. Prior to phase analysis, all XRD scans were detexturized to eliminate the influence of crystallographic orientation. Furthermore, the average crystallite size, lattice microstrain, and dislocation density were determined based on the modified Williamson–Hall (W–H) method.[46,47] The fine features of the DRA structures after Erichsen testing were also characterized by EBSD mapping.

High-speed uniaxial tensile tests were carried out by using a Gleeble 3800 simulator at a strain rate of 1.5 s^{-1}. Standard subsized tensile testing specimens were machined from the DRA plates according to the ASTM-E8 standard with dimensions as follows: a thickness of 1.3 mm, a gage length of 25 mm, a width of 6 mm, and a total length of 150 mm. Three samples were tested for each annealing condition. A high-accuracy noncontact scanning optical system was attached to the Gleeble chamber, *i.e.*, a laser micrometer, for lengthwise measurements of the tensile specimens during high-speed testing. This laser micrometer system used a high-intensity GaN long-life LED combined with an HL-CCD sensor for high-speed measurements of the lengthwise changes in the tensile sample.

Formability experiments at a high speed of 50 mm s^{-1} were conducted using the Erichsen cupping testing technique to reveal the effect of grain refinement on the stretch formability of the studied steel. The Erichsen specimens were rectangular plate with dimensions of 70 mm × 140 mm. More details of the applied parameters during Erichsen testing are found in Reference 43. The tests were repeated two times, and the Erichsen index (EI), *i.e.*, the maximum height of the cups (in mm) before fracture, was recorded.

To evaluate the adiabatic temperature rise, high-speed tensile tests were simulated on CG 301LN and DRA T800-1 structures by coupled field (structural–thermal) 3-dimensional finite-element (FE) analyses using the ANSYS commercial software package. The FEM results were experimentally compared with the temperature data recorded during high-speed tensile tests. The developed model consisted of tensile machine grips and tensile specimens with thicknesses of 1.2 mm and gage lengths of 10 mm. The machine grips were glued to the 10 × 10 mm ends of the tensile specimen. The grips were considered rigid. For the tensile specimen, elastic, plastic, and thermal properties were input into the software. A total of 5667 tetrahedral coupled field SOLID226 elements were generated in a specimen. The true stress–strain curves recorded for each material in the test at a high strain rate of 1.5 s^{-1} were input into the FE analysis as multilinear isotropic hardening data. A density of 7800 kg m^{-3}, a specific heat capacity of 490 J kg^{-1} K^{-1}, and a thermal conductivity of 15 W mK^{-1} were used for the tensile specimens. The heat generation rate was considered to be 1, *i.e.*, all the plastic work was assumed to be converted into thermal energy. A convection/film coefficient of 50 W m^{-2}K^{-1} was applied to all the external surfaces of the model. Finally, while the lower grip was constrained in all directions, the

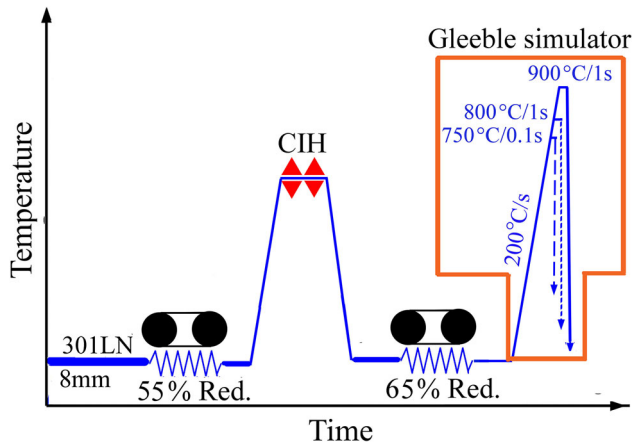

Fig. 1—Double-reversion annealing processing of the studied steel.

upper grip was set to move uniaxially at a constant speed of 0.014 m s^{-1}, corresponding to a mean strain rate of 1.5 s^{-1}.

Furthermore, the Erichsen cupping tests were also simulated by the FEM. Material properties equal to those from the tensile experiments were used in the software. For these analyses, the model was constructed according to the experimental Erichsen setup and included the strip specimen, punch, die, and blank holder. All components were considered rigid except the specimen, which included plasticity. Therefore, a fine hexagonal mesh of coupled field elements was generated in the metallic strip, which included 44,890 SOLID226 elements. The die was constrained in all directions, while the punch was moved at a constant speed of 3 m s^{-1} perpendicular to the specimen surface. A homogeneous pressure of 25 MPa was applied by the blank holder.

III. RESULTS

A. *SRA Microstructure*

In this section, the initial microstructures prior to DRA are introduced to reveal the influence of the subsequent DRA process. The as-received structure shows a coarse grain structure with an average grain size of 16 μm, as shown in Figure 2(a). A small fraction of α'-martensite, ~ 4 pct, coexisted with and was distributed inside the austenitic grains. This martensite formation in the initial structure is attributed to skin-pass deformation conducted by the supplier, *i.e.*, final surface rolling with a slight deformation of 5 to 7 pct. The material was subjected to cold-rolling deformation with a 55 pct reduction and subsequent reversion annealing at 690 °C for 60 seconds using the CIH line (see Figure 1). This single-reversion annealing (SRA) treatment promoted a fine-grained austenitic structure, as shown in Figure 2(b). The magnified view in Figure 2(c) shows that the grain structure achieved with SRA is inhomogeneous, since some regions of coarse grains of size 4 μm, highlighted by the yellow circles, are enhanced. The grain size distribution of the grain structure in Figure 2(b) is shown in Figure 2(d). Most of the grains in the SRA structure, ~ 75 pct, have a size ≥ 2 ~ μm. Consequently, the average grain size of the grain structure achieved by SRA processing is 2.7 μm.

B. *Microstructures Resulting from DRA*

The microstructural features of the microstructures resulting from DRA were analyzed by EBSD mapping. Figure 3 displays the microstructure of the 301LN steel reversion annealed at T750-0.1 by DRA. Ultrafine grains along with a small fraction of retained austenite grains are observed, as indicated by the yellow circles in Figure 3(a). The corresponding orientation map, *i.e.*, inverse pole figure (IPF), shows that the structure achieved by DRA at T750-0.1 has a textured orientation related to the grain size regime, as shown in Figure 3(b). The elongated retained austenite grain regime exhibits a ⟨101⟩ crystallographic orientation (green color); however, the new fine-grain regime shows ⟨111⟩ and ⟨001⟩ crystallographic orientations. The high-magnification image of Figure 3(c) shows a homogeneous and equiaxed ultrafine-grained structure with sharp and clear high-angle boundaries (HAGBs, > 15 deg). The grain size distributions of the UFG structure achieved at T750-0.1 are shown in Figure 3(d). It shows that 75 pct of the new grains are smaller than 0.5 μm, and 20 pct of the grains are in the 0.5–1 μm range. The estimated average grain size is 0.48 μm. The volume fraction of martensite remaining in the DRA T750-0.1 structure, as measured using XRD, was approximately 3.6 pct.

However, at a longer DRA time (1 second) and higher reversion temperature (800 °C), the microstructure is characterized by fine-equiaxed grains along with some retained elongated grains, as shown in Figure 4(a). The corresponding orientation map exhibits a similar textured orientation related to the grain size regime since the elongated retained austenite grain regime exhibits a ⟨101⟩ crystallographic orientation, as shown in Figure 4(b). Grain structure variation with different grain size regimes is promoted, as shown by the high-magnification image in Figure 4(c). The grain size distributions of the structure obtained by DRA at T800-1 are shown in Figure 4(d). It shows that 63 pct of the new grains are smaller than 0.5 μm, and 25 pct of the grains are in the 0.5–1 μm range. These grain size distributions are slightly higher than those achieved at T750-0.1. Hence, the estimated average grain size of DRA T800-1 is 0.53 μm, slightly larger than that of the DRA T750-0.1 structure. Less nonreverted α'-martensite coexisted in the structure subjected to DRA, approximately 2 pct.

As the reversion temperature increases to 900 °C, the microstructure after DRA exhibits homogenous fine-equiaxed austenitic grains, as shown in Figure 5(a). A striking feature of this structure is the disappearance of elongated retained austenite grains due to recrystallization. The orientation map shows that most of the new grains have a predominantly ⟨101⟩ textured orientation, as shown in Figure 5(b). A magnified image of the structure after DRA shows an ultrafine-grained structure with few large grains, as shown in Figure 5(c). The grain size distributions of the structure achieved after DRA at T900-1 are shown in Figure 5(d). DRA T900-1 contains fewer ultrafine grains of sizes < 0.5 μm than DRA T750-0.1 and DRA T800-1, with approximately 55 pct of the new grains being smaller than 0.5 μm, and 30 pct of the grains being in the 0.5–1 μm range. Consequently, the average grain size of DRA T900-1 is 0.75 μm, slightly larger than that of the DRA T800-1 structure.

The texture of the structures processed by DRA at different temperatures and times was evaluated by EBSD analysis. The texture patterns of the structures after DRA are presented by the constant $\phi 2 = 0$ and 45 deg ODF sections for the austenitic matrix, as shown in Figure 6. The structure after DRA mainly comprises a strong brass component {011}⟨112⟩. In addition, two texture components, Goss{110}⟨001⟩ and Cu {112}⟨112⟩, are present. There is a drastic decrease in

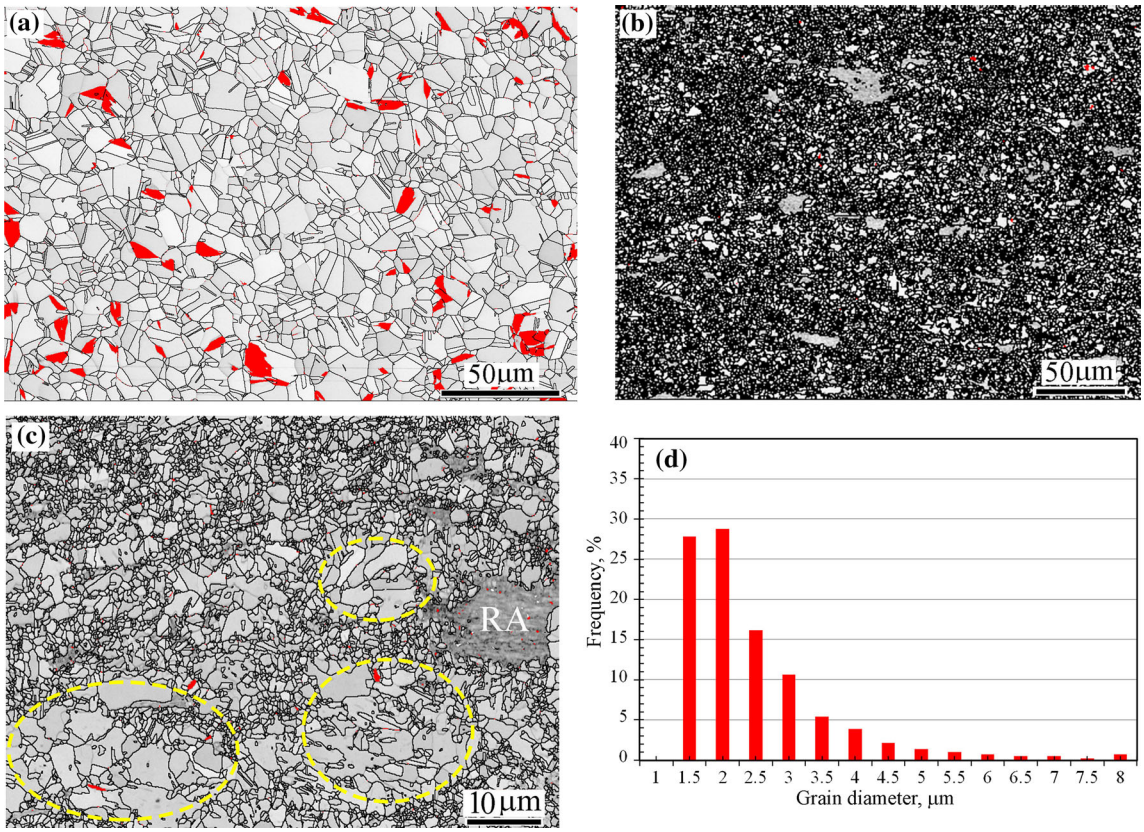

Fig. 2—EBSD-imaging maps showing microstructure evolution of the initial structures before double-reversion annealing: (*a*) as-received microstructure (EBSD-IQ map superimposed with the phase map; α'-martensite shown in red), (*b*) single-reversion annealing microstructure achieved by annealing at 690 °C for 60 s, (*c*) high-magnification view of (b), and (*d*) grain size distribution for the corresponding grains in (b) (Color figure online).

the overall intensity of the texture with increasing reversion annealing temperature to 900 °C. The texture of DRA T900-1 is nearly 1/2 of that of the previous structures after DRA. It has been reported that the brass texture component is the major texture pattern in low-SFE materials of austenitic structures, such as austenitic stainless steel and TWIP steels.[48,49] The strong brass texture component of the DRA T750-0.1 and T800-1 structures appeared to be related to proficient shear banding.[50]

C. *High-Speed Tensile Properties*

The tensile properties of the structures subjected to DRA at room temperature were measured at a high strain rate of ~ 1.5 s^{-1} corresponding to the high punching speed of 50 mm s^{-1} applied in the Erichsen tests for the same structures. Figure 7(a) shows the engineering stress–strain curves of the CG 301LN and specimens subjected to DRA at different temperatures and times. The mechanical properties extracted from the flow curves, such as the yield strength $R_{0.2}$, tensile strength R_m, and total elongation E_{tot}, are listed in Table I. The DRA T800-1 and T900-1 structures exhibit $R_{0.2}$ values of 950 and 770 MPa, respectively, which are significantly higher than the $R_{0.2}$ of CG 301LN (≈ 420 MPa). The total elongations of both structures are perfectly adequate, 35 and 40 pct. These values are comparable with those of CG 301LN. However, the DRA T750-0.1 structure reveals a very low elongation of ~12 pct and displays discontinuous yielding. The value of the yield drop, *i.e.*, the difference between the upper and lower yield stresses, is ~100 MPa. This discontinuous yielding of the T750-0.1 structure is attributed to the high dislocation density and the anchored dislocations due to the carbon–dislocation interactions, as explained by Cottrell–Bilby theory.[51] The occurrence of discontinuous yielding in grain-refined steels is a common phenomenon. As discussed by Song *et al.*,[52] discontinuous yielding has been frequently observed in UFG ASSs, while their coarse-grained counterparts exhibit continuous yielding. Thus, a fine submicron/micron grain size is an essential factor. As seen in Figure 7(a), the coarse-grained 301LN steel shows continuous yielding and prominent strain hardening. However, the strain hardening decreases in structures after DRA, and Lüders strain becomes evident at an annealing temperature of 800 °C, *i.e.*, with refined grain size. The same trend is seen in the stress–strain curves reported in Reference 30.

At 800 °C, a slight discontinuous drop in the yield strength of ~10 MPa followed by a Lüders strain plateau without strain hardening is observed. Consequently, the strain hardening at the Lüders plateau strain reaches

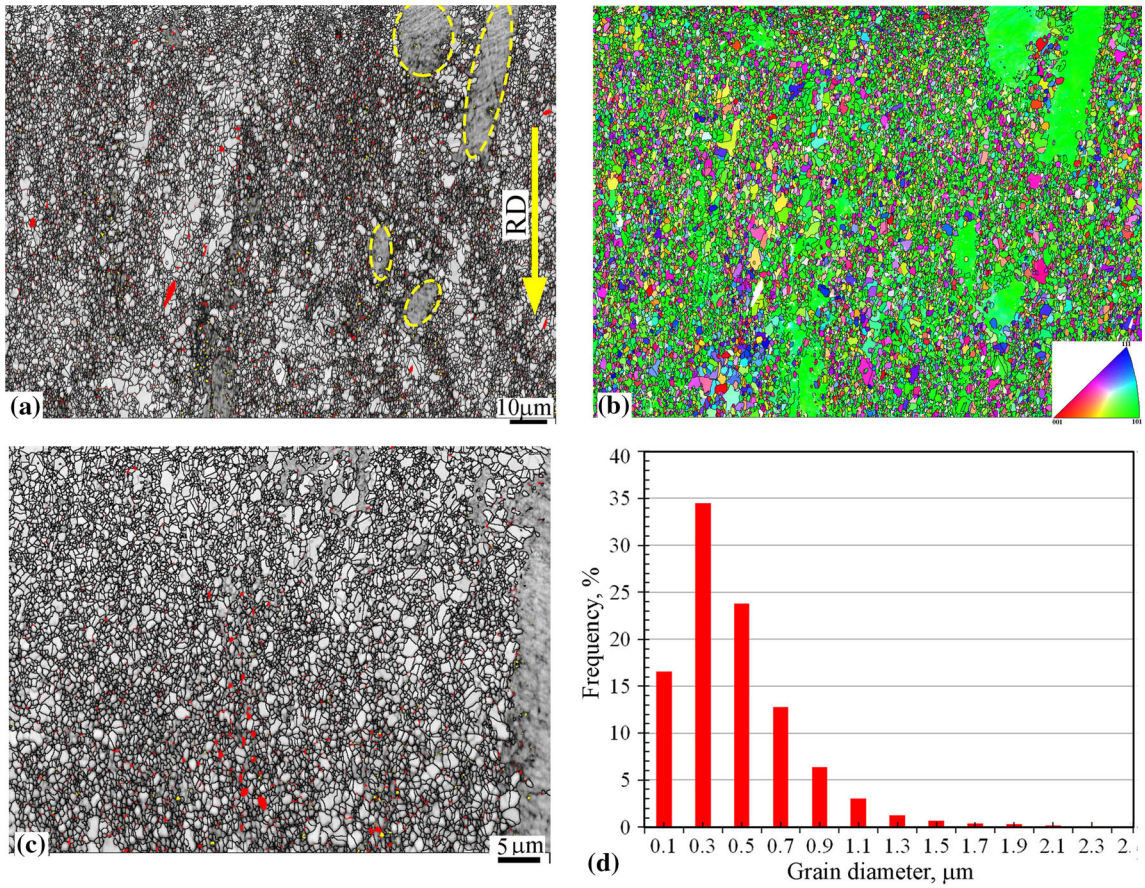

Fig. 3—Microstructure after double revision annealing at 750 °C for 0.1 s: (*a*) EBSD-IQ map superimposed with the phase map (α′-martensite shown in red), (*b*) EBSD orientation map of (a), (*c*) high-magnification IQ map, and (*d*) grain size distribution for the corresponding grains in (c), showing the finest reverted austenitic grains, with grains smaller than 500 nm (*RD* rolling direction, marked by the yellow arrow) (Color figure online).

zero, as shown in Figure 7(b). The slightly discontinuous yielding in the DRA T800-1 structure is attributed to the weak carbon–dislocation interactions. At a higher DRA temperature of 900 °C, the discontinuous yielding was fully eliminated. This is attributed to interstitial C atoms being either absent due to carbide precipitate formation or weakly interacting with the recovered dislocations.[53]

The temperature rise of the tested specimens was measured during high-strain rate tensile testing using a fixed thermocouple. Due to adiabatic heating, the temperatures increased to 126 and 136 °C at the end of the tensile test for DRA T900-1 and DRA T800-1, respectively. This will be further discussed in Section 4.

Figure 7(b) shows the corresponding strain-hardening rate (SHR) curves of the structures after DRA. The SHR of the CG structure, plotted in black, is higher than the SHR of the structures after DRA. The soft γ-matrix of CG 301LN is significantly hardened due to the formation of shear bands, *i.e.*, highly strained regions with a high density of dislocations and strain-induced α′-martensite plates formed at shear bands. Hence, the SHR of the soft γ-matrix of CG 301LN is higher than the SHRs of the hard γ-matrix of the structures after DRA. In agreement, Hamada *et al.*[33] found that UFG 301LN with a grain size ~ 0.75 μm exhibited a lower SHR than CG 301LN. Mandal *et al.*[54] reported that the CG structure of 301L showed substantial strain hardening, whereas fine- and ultra-fine-grained structures developed by reversion annealing at 750 °C for 1 to 2 minutes and 700 °C for 10 minutes hardly strain hardened. A striking feature of the SHR of DRA T750-0.1 is the considerable drop below zero. This drop in SHR to a negative value usually indicates the start of necking according to the criterion of necking.[55,56] However, plastic instability associated with necking does not occur at this strain. This remarkable drop in SHR is attributed to discontinuous yielding, as shown in the corresponding flow curve in Figure 7(a). It is well reported that the discontinuous yielding of reversion-annealed structures induces a sharp decrease in SHR.[57]

D. *Microstructural Evolution of DRA Structures After Tensile Testing at High Speed*

The deformation mechanism during tensile straining of the structures after DRA at a high strain rate of 1.5 s^{-1} was studied using EBSD examinations. Figure 8 shows the EBSD phase maps of the deformed DRA T750-0.1, DRA T800-1, and DRA T900-1 structures.

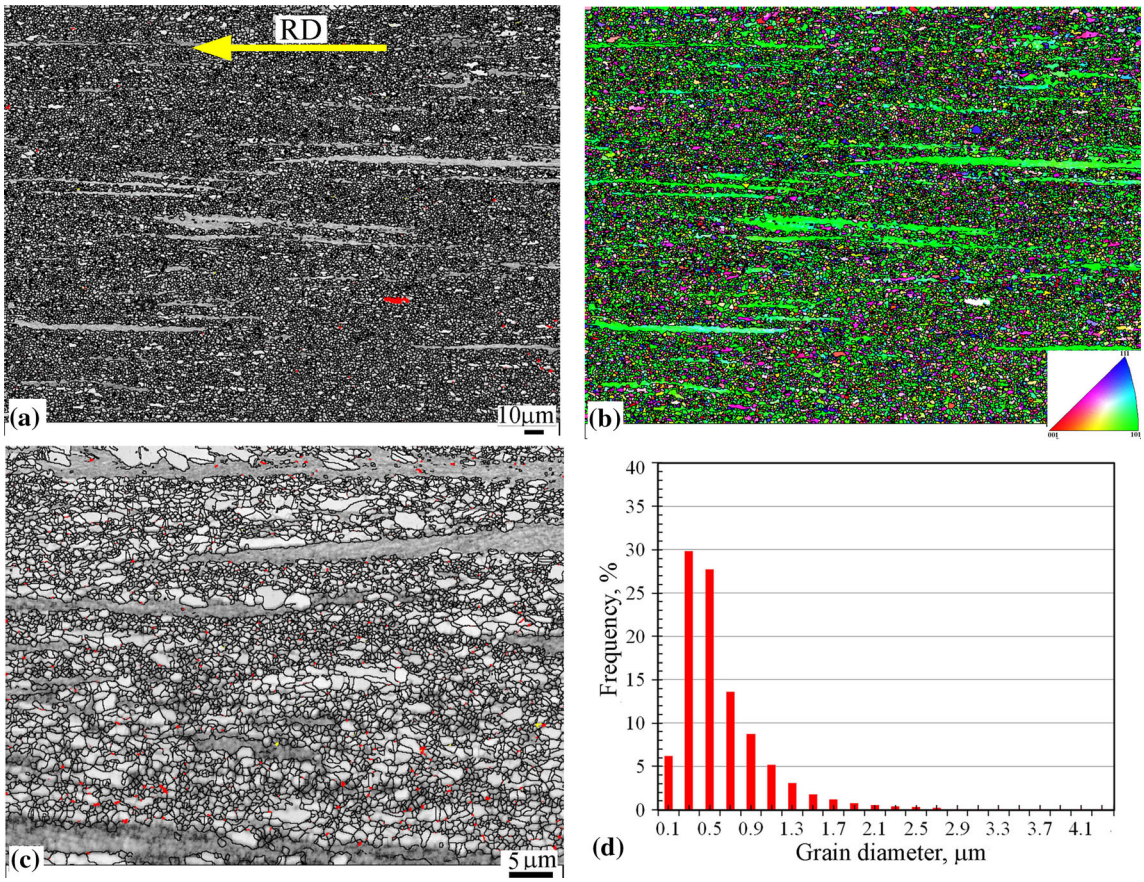

Fig. 4—Microstructure of structure subjected to double revision annealing at 800 °C for 1 s: (*a*) EBSD-IQ map superimposed with the phase map (α'-martensite shown in red), (*b*) EBSD orientation map of (a), (*c*) high-magnification IQ map, and (*d*) grain size distribution for the corresponding grains in (c), showing the finest reverted austenitic grains, with grains smaller than 600 nm (*RD* rolling direction, marked by the yellow arrow) (Color figure online).

High-speed deformation is accompanied by α'-martensitic transformation. A striking feature of the high-speed tensile deformation of the structure after DRA is the increased degree of martensitic transformation and an ultrafine-grained structure, as shown in Figure 8(a). A significant fraction of γ martensite transforms to α' martensite, ~70 pct, in DRA T750-0.1. In the magnified view shown in Figure 8(b), the γ-ultrafine grains are fully transformed into α'-grains. Figure 8(c) shows the deformed microstructure of DRA T800-1. The fraction of α'-martensite decreases to 45 pct. The high-magnification image in Figure 8(d) shows that the α'-martensitic transformation is favorable in the γ-ultrafine grains of size ~500 nm, as indicated by the yellow circles, whereas the α'-martensitic transformation does not occur in the γ-grains of size 1 to 2 μm, as marked by the white circles.

The deformed DRA T900-1 microstructure shows a completely comparable trend in α'-martensitic transformation, which reveals a significant decrease in α'-martensite fraction to 25%, as shown in Figure 8(e). As observed in Figure 8(f), most of the reverted γ grains did not transform into α'-martensite during tensile straining at high speed.

E. *Erichsen Cupping Tests*

The maximum punch stroke displacement before cracking, *i.e.*, limiting dome height (LDH) or Erichsen index (EI), has traditionally been used as a stretch formability parameter that indicates the ability to manufacture a material with the desired geometry. It is well known that the EI and the applied force in Erichsen cupping testing strongly depend on the sheet thickness and punch diameter.[58,59] In the present study, the sheet thickness and punch diameter were constant in all tests.

High-speed stretch formability tests of the structures after DRA were conducted at ambient temperature using the conventional Erichsen cupping test procedure. Figure 9(a) presents the punch stroke displacement (X) *vs* force (F) curves. At the early stage of deformation, the average forces applied to achieve a stroke displacement of 2 mm are 4 and 10 kN for the CG and DRA T800-1 structures, respectively. As deformation proceeds, the applied force increases gradually up to maximum values of 52 and 74 kN for those structures. Thus, the force required for straining is much higher for structures resulting from DRA than for CG 301LN structures. In agreement, Saray *et al.*[60] reported that the maximum load at the EI significantly increases for

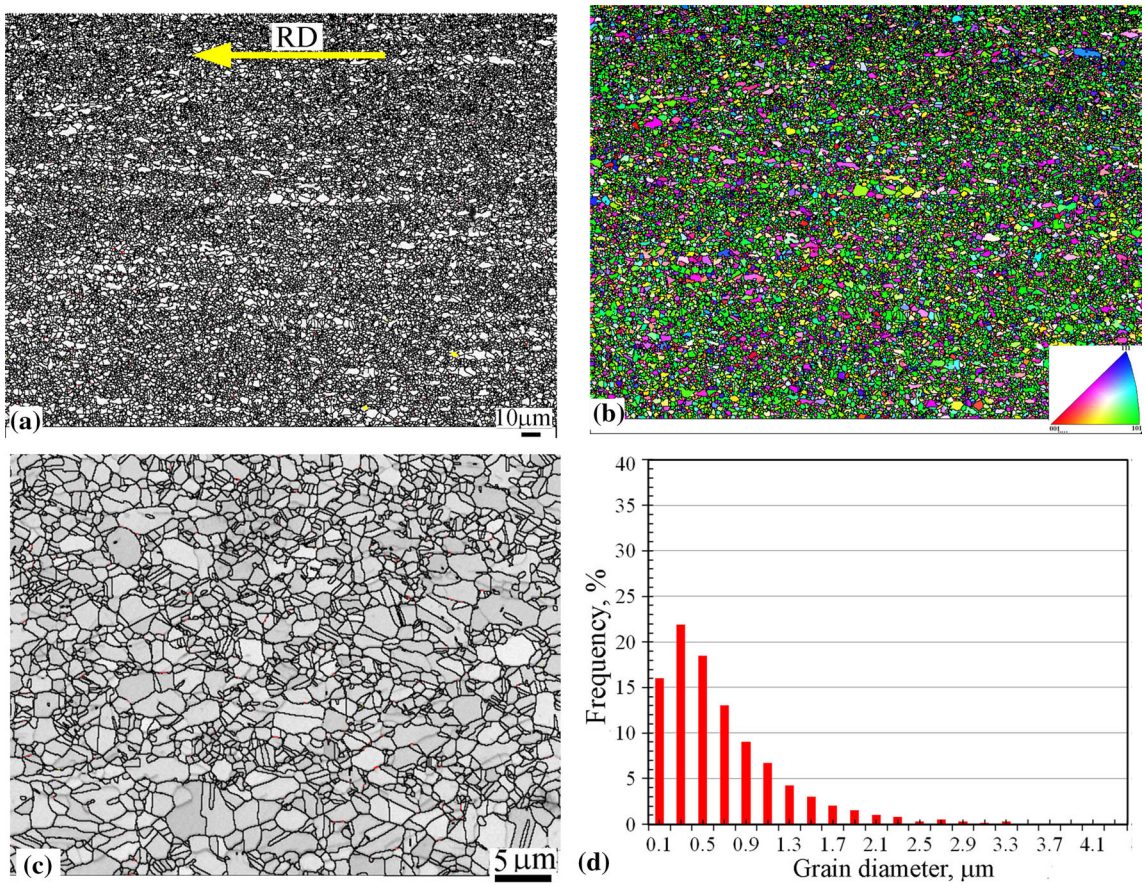

Fig. 5—Microstructure of the structure after double revision annealing at 900 °C for 1 s: (*a*) EBSD-IQ map superimposed with the phase map (α'-martensite shown in red), (*b*) EBSD orientation map of (a), (*c*) high-magnification IQ map, and (*d*) grain size distribution for the corresponding grains in (c), showing the finest reverted austenitic grains, with grains smaller than 800 nm (*RD* rolling direction, marked by the yellow arrow) (Color figure online).

UFG structures of an IF steel processed by equal channel angular pressing.

A striking feature of the deformation behavior of the structures resulting from DRA and CG 301LN under biaxial straining in the Erichsen tests at high punching speeds is the significant variation in the strain-hardening capacity, as indicated by plotting the first-order derivative of the punch force with respect to the displacement, dF/dX *vs*. X curves, as shown in Figure 9(b).

In the early stage of punching travel, the onset of deformation is governed by both Young's modulus and the strength of the structure. Hence, the DRA T750-0.1 structure exhibits the highest dF/dX at the beginning of punch travel, as indicated by the arrow. Each dF/dX-X curve exhibits a minimum peak. This peak is related to the start of yielding and plastic deformation. CG 301L exhibits the lowest peak value at early displacement in accordance with it having the lowest $R_{0.2}$. The structures resulting from DRA display higher minimum peak values and higher displacements, which can be attributed to the superior $R_{0.2}$ of the structures resulting from DRA, as seen from the tensile properties in Figure 7(a). dF/dX increases with further increasing displacement up to a maximum. In this stage, the deformation characteristic is membrane stretching and straining, where the specimen sheet becomes thinner under the effect of biaxial tensile stresses acting on the dome wall.[61] The effect of the refined grain structure obtained by DRA on the membrane thinning regime under biaxial deformation is obvious. For instance, the CG 301LN structure exhibits a long regime of 8 mm (shown by the blue arrows), whereas the DRA T800-1 structure displays a shorter regime of 4.6 mm (shown by the yellow arrows). This will affect microstructural evolution during Erichsen cupping testing, as discussed in Section 4. After further punching beyond the maximum peak, the force decreases with displacement due to crack initiation and propagation on the dome surface, promoting deformation localization. Subsequently, fracture occurred at the hemispherical dome, resulting in different EI values. This means that the fracture strains of the studied structures are different since the true strain (ε_T) at the fracture of the hemispherical dome is correlated with the EI according to Eq. [1][62]:

$$\varepsilon_T = 0.35\left(\frac{EI}{r_P}\right), \qquad [1]$$

where r_P is the punch radius (10 mm in the present work). Hence, for CG 301LN and DRA T800-1

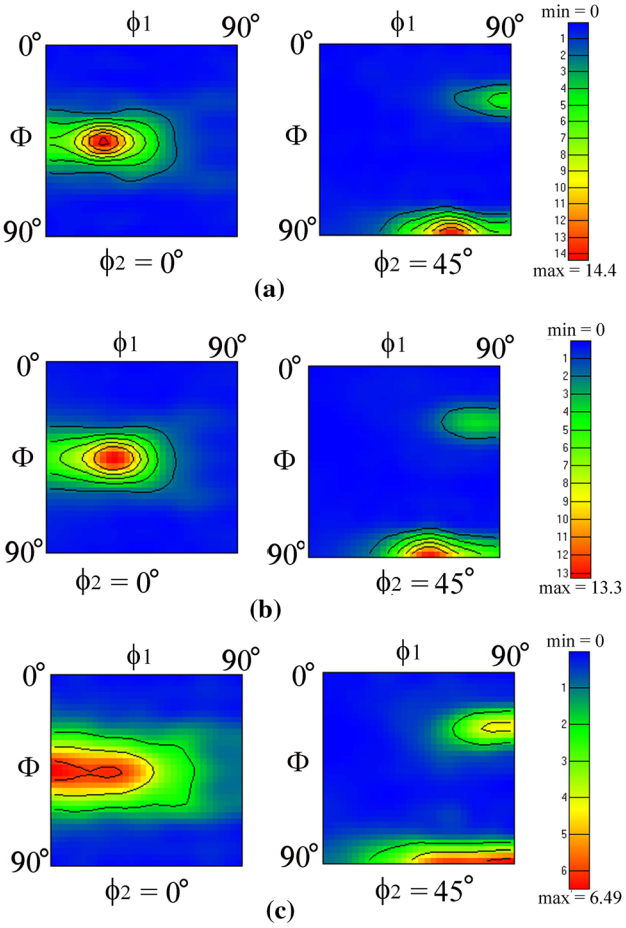

Fig. 6—ODF texture patterns at the $\phi_2 = 0$ and 45 deg sections for the austenite matrix of the structures after DRA: (*a*) T750-0.1, (*b*) T800-1, and (*c*) T900-1.

structures, EI = 12.5 and 10.6 mm, and the true failure strains are 0.44 and 0.37, respectively.

The EI values from the high-speed Erichsen tests (HSs) are plotted as a function of the $R_{0.2}$ of the structures resulting from DRA. In Figure 10, the EI values measured with low-speed tests (LSs), taken from Reference 37, are given for comparison. Although grain refinement in the structures resulting from DRA significantly improves the mechanical strength, their EI values are almost comparable with those of the coarse-grained structure. In addition, with increasing punch speed from quasi-static to high speed, the EIs of the studied structures are only slightly decreased. For instance, by promoting the grain refinement of DRA T800-1, $R_{0.2}$ increased by 140 pct, while the corresponding EI decreased by 10 pct at a low punching speed. Similarly, at a high punching speed, the $R_{0.2}$ of DRA T800-1 increased by 125 pct, and the EI decreased by 15 pct.

F. *Microstructural Changes and Associated Deformation Mechanism During High-Speed Erichsen Testing*

The EBSD image quality (IQ) map together with the corresponding phase map of the deformed CG structure during high-speed Erichsen testing is shown in Figure 11. From the variation in IQ in Figure 11(a), the formation of dislocation substructures within the strained regions inside the grains can be concluded. According to the literature, the most significant feature of the uniaxial deformation of CG 301LN is shear bands.[2,63] Since the strain field of these bands is significantly high due to the high density of dislocations, martensitic transformation is induced in these bands. Hamada *et al.*[64] found that deformation strain is localized at the grain boundaries of TWIP steels during

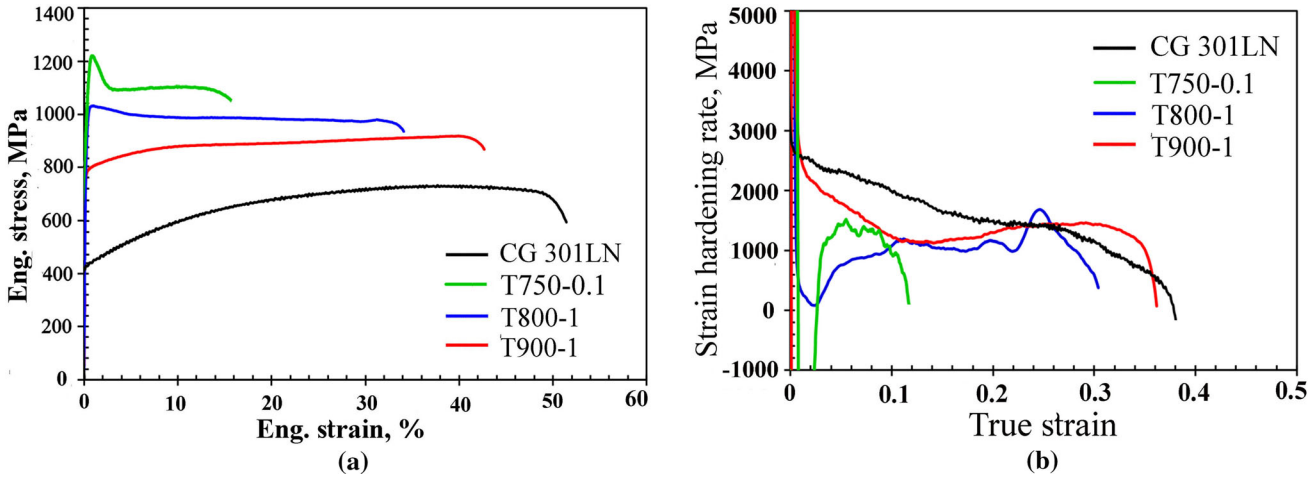

Fig. 7—Tensile mechanical properties of the structures subjected to DRA at room temperature: (*a*) engineering stress–strain curves and (*b*) strain-hardening rate curves of the structures subjected to DRA at room temperature and a high strain rate of 1.5 s^{-1}.

biaxial deformation in Erichsen testing. The phase map in Figure 11(b) shows that the martensitic transformation was strongly activated under biaxial straining in Erichsen testing so that the austenitic structure of the CG 301LN steel was almost completely transformed to α'-martensite, approximately 98.8 pct.

Figure 12(a) shows the IQ map of DRA T800-1 after high-speed Erichsen deformation, revealing distinct local differences caused by existing martensitic and austenitic regions, as seen from the EBSD phase map (Figure 12(b)). Thus, there is ~ 42 pct martensite and 58 pct austenite in the strained structure. The martensite fraction is higher than the 33% measured after tensile testing, indicating that higher martensite fractions formed in biaxial straining than in uniaxial tensile straining, as reported earlier.[43] On the other hand, this shows that the structure grain-refined by DRA is less prone to martensite transformation during the high-speed Erichsen test. This is attributed to the longer thinning deformation regime, 8 mm, of the CG structure under stretching and straining, whereas the DRA T800-1 structure exhibited a shorter thinning deformation regime of 4.6 mm (see Figure 9(b)).

The austenite and martensite contents of the Erichsen-tested specimens were also measured by XRD. The corresponding X-ray diffraction patterns are presented in Figure 13. The martensite and austenite phase fractions of the CG 301-HS (HS = high speed) specimen were 98.8 and 1.2 pct, respectively, whereas the corresponding phase fractions were revealed to be 45.2 pct martensite and 54.8 pct austenite in the DRA T800-1 (UFG-HS) specimen.

Furthermore, to quantify the dislocation density of Erichsen-tested CG-HS and UFG-HS specimens, the average lattice strain and crystallite size of both austenite and martensite phases were first determined from the average peak broadening of the (111), (200), (220), (311) and (222) reflections for austenite and the (101), (200), (211) and (202) reflections for martensite using Scherrer's equation,[46,65] and the dislocation density of the corresponding phases was estimated by the modified W–H method using the following equation[47]:

$$\left\{\Delta K^2 - (0.9/D)^2\right\}/K^2 \cong \beta\overline{C}_{h00}(1 - \mathrm{qH}^2) \qquad [2]$$

where D is the average crystallite size, ΔK is the full width at half maximum (FWHM), $K = (2\sin\theta)/\lambda$, λ is the wavelength (0.15406 nm for Cu-Kα), and θ is the diffraction angle. $\beta = \pi\rho M\ ^2b^2\ /\ 2$, where ρ is the dislocation density, M is a constant depending on both the effective outer cutoff radius of dislocations and the dislocation density (usually taken as 2[66,67]), and b is the magnitude of the Burgers vector (0.254 nm and 0.249 nm for austenite and martensite, respectively[68,69]). C_{h00} is a constant corresponding to the elastic constants of $C11$, $C12$, and $C44$ based on the elastic anisotropy, expressed as $A_i = 2C_{44}/(C_{11} - C_{12})$, $H^2 = (h^2k^2 + h^2l^2 + k^2l^2)/(h^2 + k^2 + l^2)$, where h, k, and l are Miller's indices of each peak and q is a parameter indicating the dislocation character of the samples. The values of $C11$, $C12$, and $C44$ are 248, 110, and 120 for martensite, respectively, and 209, 133, and 121 GPa for austenite, respectively.[70,71] To obtain the value of q, the linear plot of $\{\Delta K^2 - (0.9/D)^2\}/K^2$ *vs* H^2 for all the considered reflections was used. Afterward, the slope of the plot of ΔK^2 *vs* $K^2C_{h00}(1-qH^2)$ for all the considered reflections was used to obtain the value of β. The values of the calculated lattice microstrain crystallite size, dislocation density and other constants are summarized in Table II.

The calculated microstrain of the Erichsen-tested UFG-HS specimen was found to be relatively higher than that in the CG-HS specimen. This is further corroborated by the calculated dislocation density. The accumulation of a relatively large amount of microstrain in the UFG-HS specimen yields a relatively high degree of strain-induced martensitic transformation from austenite. Note that the dislocation density of both CG-HS and UFG-HS specimens obtained after the high-speed Erichsen test is lower than that obtained after the low-speed Erichsen tests.[43] This is naturally attributed to adiabatic heat evolution during the high-speed test, resulting in significant dislocation recovery.

G. *Fracture Surface Features*

SEM micrographs representing the free dome surfaces and fracture surfaces through the thickness of DRA T750-0.1 and DRA T800-1 samples after the Erichsen tests are shown in Figure 14. The surface cracks extend on the dome surface following the paths of the strain localization bands, as shown in Figures 14((a) and (b)). It is generally accepted that the intense deformation of grain-refined 301LN is accommodated at grain boundaries and shear bands formed during stretching deformation in Erichsen testing.[72] Meanwhile, the orange peel effect associated with stretching deformation affects the surface roughness of the stretched cups.[73] This is illustrated by the irregularity of the surfaces of the stretched cups. Based on the measurements of the surface roughness parameter R_Z of electropolished CG 301L and DRA T800-1 specimens, the stretched surface of CG 301LN exhibited a considerable R_Z value of 10 μm, whereas the very smooth the surface of DRA T800-1 was characterized by a lower R_Z ~ 3 μm.

The fracture surface through the thickness of DRA T750-0.1 after the Erichsen test is shown in Figure 14(c). Distinct zones of micro/nanoscale dimpled features and relatively flat quasi-cleavage facets with tiny tear ridges, marked by yellow circles, are the features of the fracture morphology. Normally, the fracture surface of the hard-martensitic phase typically exhibits a flat-shaped fracture morphology.[74] The flat "cleavage-like" pattern is evidence of martensite in DRA T750-0.1. In contrast, the morphology of the fracture surface of DRA T800-1 after the Erichsen test is clearly ductile, displaying dimple features, as shown in Figure 14(d). The dimpled fracture surface and multiple secondary cracks are clearly visible in the SEM image shown in Figure 14(e) taken at higher magnification. The present observations reveal that secondary cracks form along the grain boundaries within the localized deformation bands.

Table I. Mechanical Properties of the Structures After DRA, Obtained by Performed High-Speed Tensile Tests at a Strain Rate of 1.5 s^{-1} (~ 50 mm s^{-1}):

Structure	GS (μm)	YS ($R_{0.2}$) (MPa)	TS (R_m) (MPa)	El_{tot}(%)
DRA T750-0.1	0.48	1100 ± 24	1228 ± 22	12 ± 3
DRA T800-1	0.53	950 ± 22	1050 ± 18	35 ± 5
DRA T900-1	0.75	770 ± 18	950 ± 20	40 ± 4
CG 301LN	16	420 ± 12	735 ± 14	48 ± 3

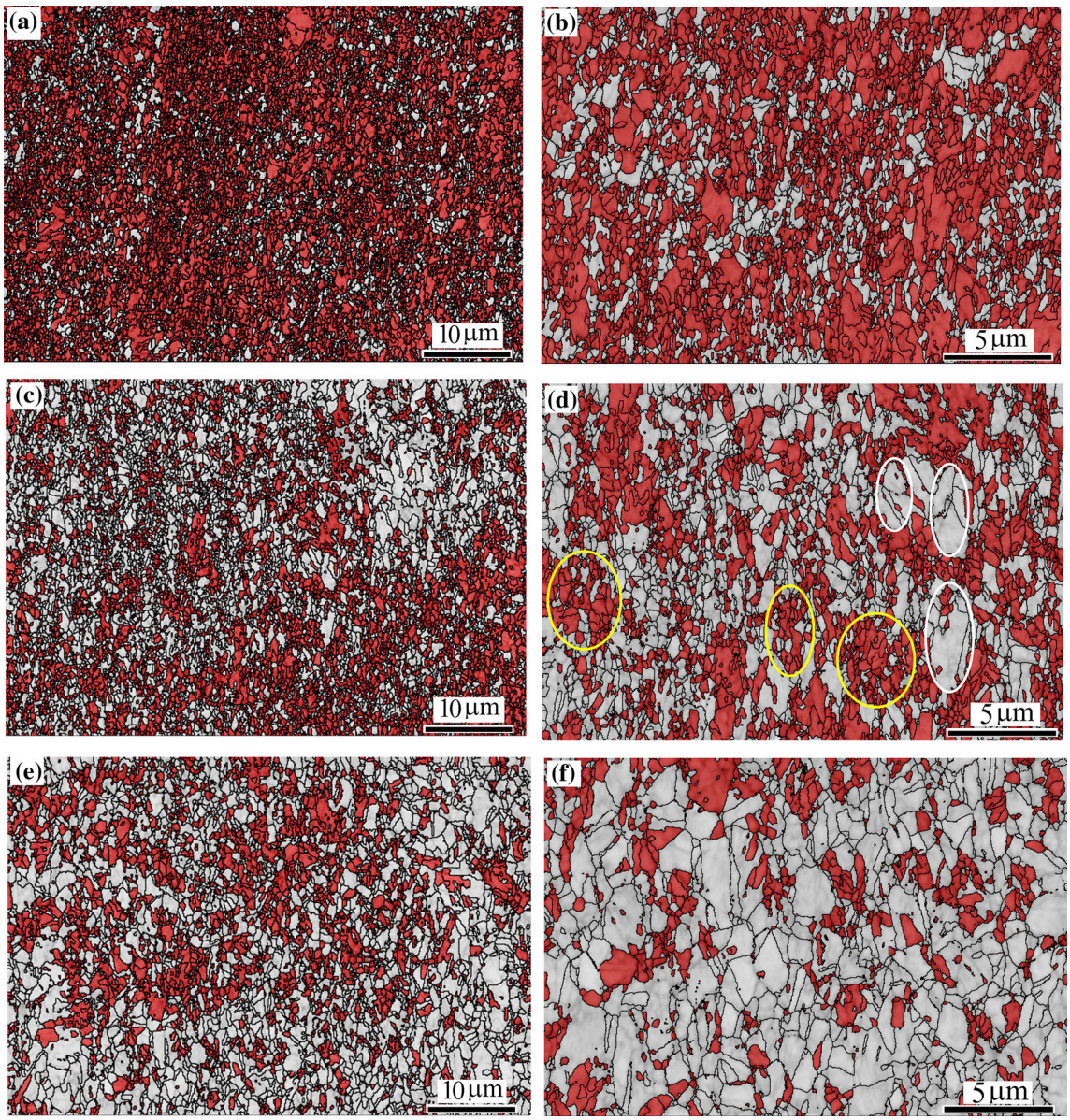

Fig. 8—EBSD phase maps showing the microstructures of samples subjected to DRA until failure under high-speed tensile testing at a strain rate of 1.5 s^{-1} (~ 50 mm s^{-1}): (*a*) DRA T750-0.1, (*b*) a magnified view of (a), (*c*) DRA T800-1, (*d*) a magnified view of (c), (*e*) DRA 900-01, and (*f*) a magnified view of (e). The EBSD maps show α'-martensite in red and austenite in gray (Color figure online).

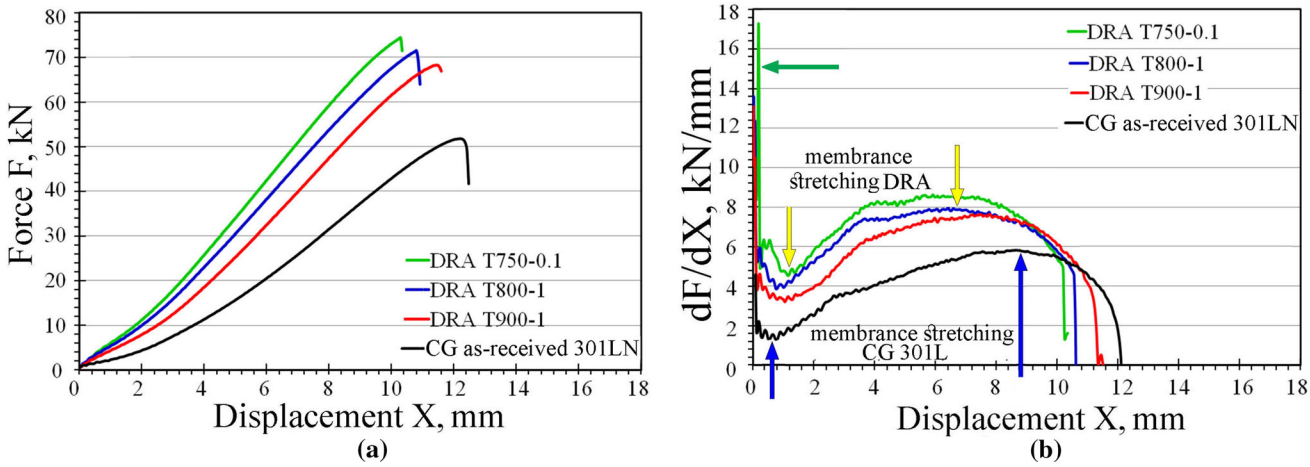

Fig. 9—Force *vs* displacement (*F–D*) curves of stretch formability tests of structures resulting from DRA using Erichsen cupping testing at a high speed of 3000 mm min^{-1}.

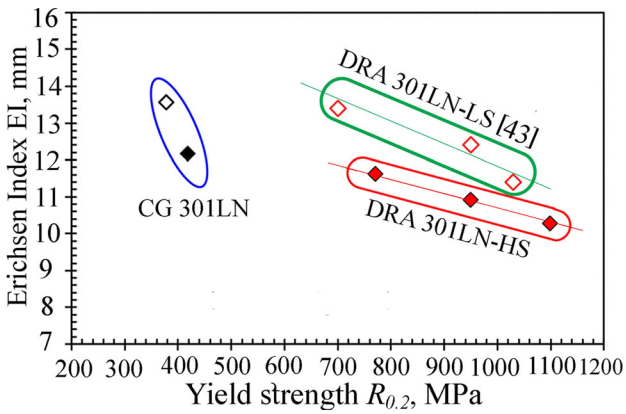

Fig. 10—Dependence of the Erichsen index (EI) on the YS of the structures resulting from DRA and CG 301LN structure at a high punching speed of 3000 mm min^{-1} (solid symbols). For comparison, EI values of CG 301LN and DRA 301LN at a low punching speed of 30 mm min^{-1} (open symbols) are included, taken from Ref. [43].

IV. FINITE ELEMENT ANALYSIS OF DEFORMATION

The plastic deformation in the CG 301LN and DRA T800-1 structures was simulated by the FEM using the ANSYS software package.

A. *Tensile Tests*

The contours of Von Mises equivalent strain at the end of high-speed tensile tests (the failure point determined from experimental flow curves) are obtained by FEM analysis and are demonstrated in Figure 15. Necking is obvious in both specimens, leading to higher local strains in the middle.

The distributions of true strain along the gage length of the specimen in various instances are plotted in Figure 16. The strain in the CG 301LN specimen remained uniform up to true strains as high as ~ 0.25,

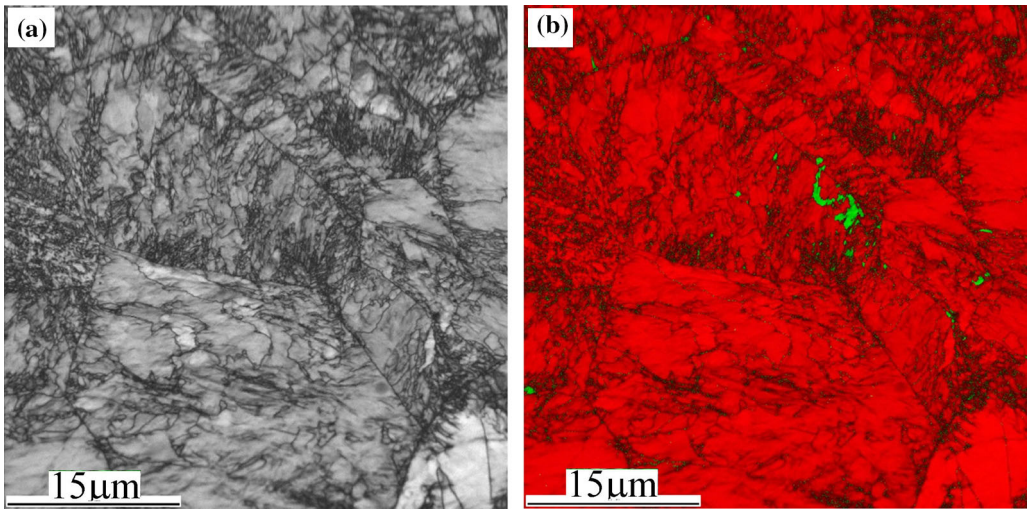

Fig. 11—EBSD results: (*a*) IQ map and (*b*) phase map of CG 301LN after stretch formability deformation by the high-speed Erichsen test. Austenite is shown in green and martensite is shown in red in (b) (Color figure online).

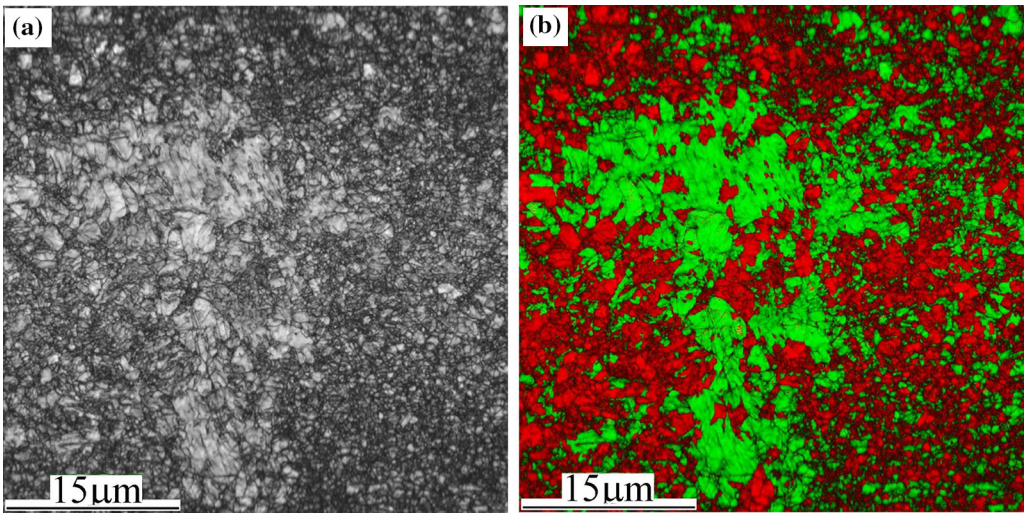

Fig. 12—EBSD results: (*a*) IQ map and (*b*) phase map of DRA T800-1 after stretch formability deformation by the Erichsen test.

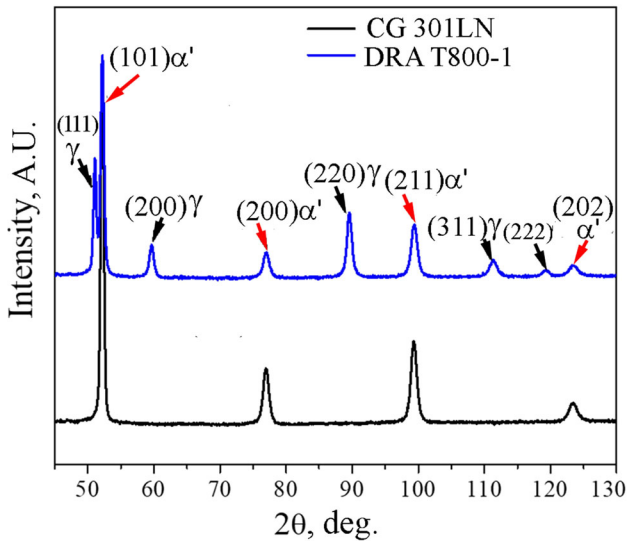

Fig. 13—XRD patterns of the CG 301LN and DRA T800-1 structures deformed under high-speed Erichsen testing.

although strain localization was observed at the end of the test (0.26 seconds from the beginning). However, localization initiated in the reversion-annealed specimen after ~0.15 s and severely increased 0.2 seconds from the beginning of the test.

The slightly different strain profiles of the two specimens can be explained by their strain-hardening capabilities. As shown in Figure 7(b), the CG specimen showed a high hardening rate of ~ 2000 MPa from the beginning of the test until a true strain of ~ 0.2 was reached. A lower hardening rate was observed for DRA T800-1, although it slightly increased with increasing deformation. On the other hand, previous work has shown that the extent of strain-induced martensitic transformation increases faster in the DRA specimen than in the CG counterpart for quasi-static deformation of the same steel.[43] Thus, the lower strain-hardening rate encountered here in the high-speed deformation of the UFG material can be at least partly ascribed to its much higher initial yield stress. In other words, the very high lattice frictional stress in this ultrafine-grained

Table II. Microstructural Characteristics of the CG-HS and UFG-HS (T800-1) Structures After Stretching by High-Speed Erichsen Tests by Subjected the XRD Data to Rietveld Refinement

Structure	Phase	Phase Fractions (Pct)	Crystallite Size (nm)	Dislocation Density ($\times 10^{14}$ m^{-2})	q	M	β (Pct)
CG at HS	α	98.8	271±5	0.7±0.2	1.74	2.3	0.32
	γ	1.2	—	—	—	—	—
UFG at HS	α	45.2	198±3	2.3±0.2	2.15	1.6	0.68
	γ	54.8	462±2	0.9±0.2	1.8	2.1	0.38

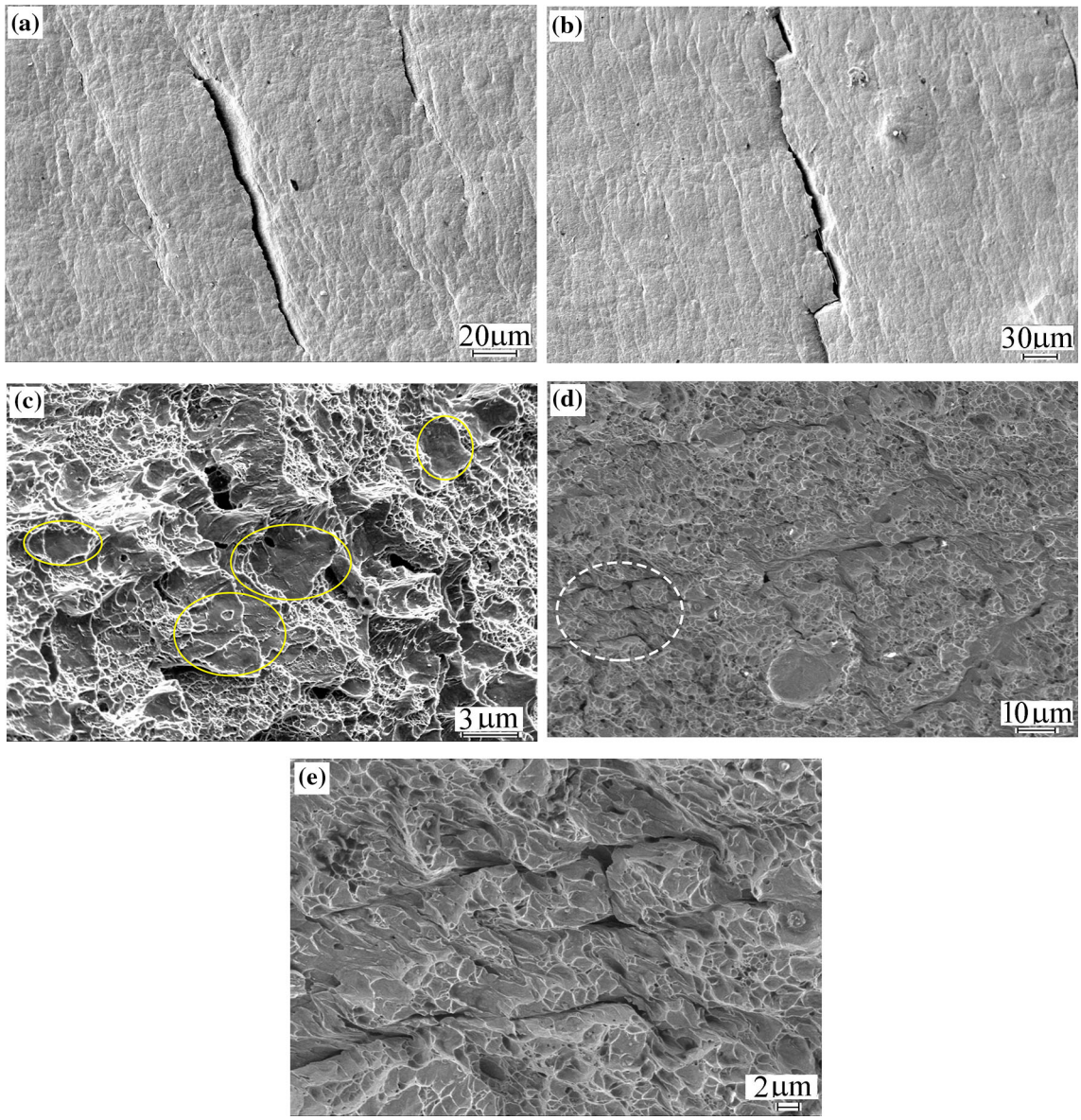

Fig. 14—FEG-SEM fractographs of the surfaces of the structured resulting from DRA after high-speed Erichsen testing: (*a*) and (*b*) surface cracks on the top of the hemispherical dome of DRA T750-0.1 and DRA T800-1, respectively, (*c*) mixed mode fracture morphology of DRA T750-0.1, (*d*) dimple fracture morphology of DRA T800-1, and (*e*) a magnified view of the fracture surface in (d).

specimen diminishes the influence of isotropic hardening. Furthermore, due to its higher yield stress, the specimen subjected to DRA exhibits an adiabatic temperature rise that is initially more pronounced than that exhibited in the CG material. This can greatly affect the SFE of the material and, hence, its mechanical behavior, as will be further discussed in this section.

It is well known that high-speed deformation of materials is an adiabatic process that increases the temperature of the material and, hence, influences its mechanical behavior. The temperature rise (ΔT) can be calculated by a balance of thermal and mechanical energies through the following general relationship:

$$Q = mc\Delta T = \beta W, \qquad [3]$$

where Q is the generated heat, m is the mass, c is the specific heat capacity, W is the total deformation work applied to the material, and β is usually considered the part of the mechanical work that is transformed into heat (also known as the Taylor–Quinney coefficient). Dividing both sides of Eq. [3] by volume gives

$$\Delta T = \frac{\beta}{\rho c} \int \sigma \mathrm{d}\varepsilon, \qquad [4]$$

where ρ is the density of the material, σ and ε are the flow stress and strain, respectively, and $\int \sigma \mathrm{d}\varepsilon$ is equal to the deformation work per unit volume.

The temperature contours for the high-rate tension of CG specimens and specimens subjected to DRA at the failure strain, which are calculated by the

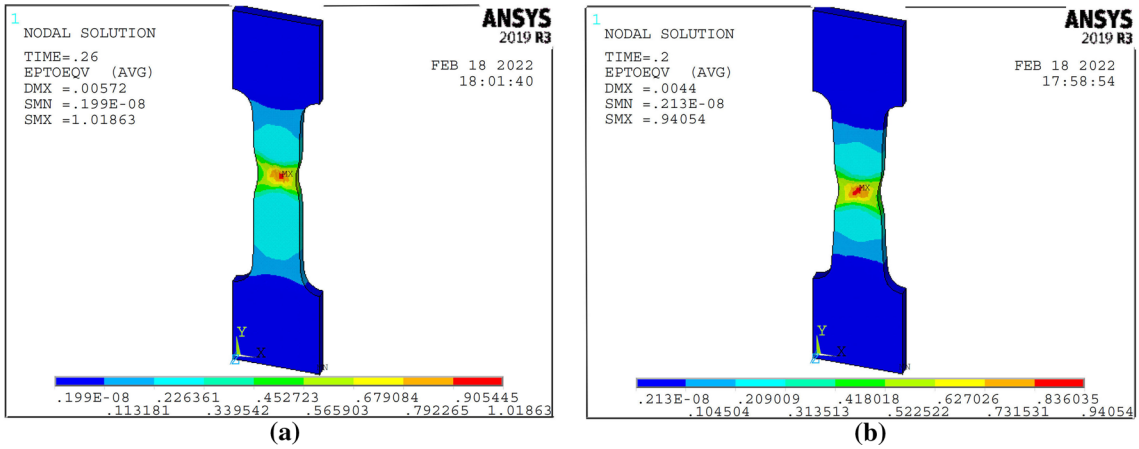

Fig. 15—Contours of Von Mises strain at the end of tensile tests determined for (*a*) CG 301LN and (*b*) DRA T800-1 structures.

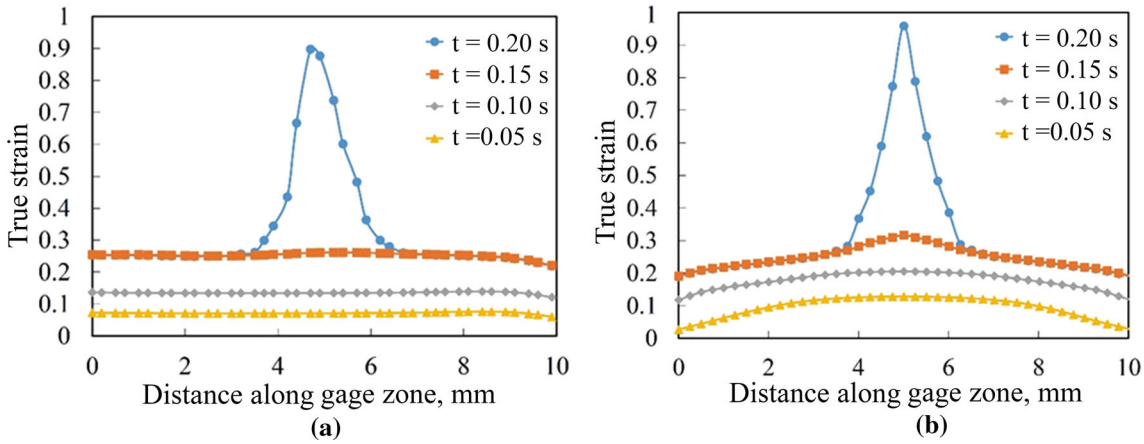

Fig. 16—True strain profiles of (*a*) CG 301LN and (*b*) DRA T800-1 structures during tensile testing for various instances.

thermomechanical coupled field FEM analyses, are presented in Figure 17. Expectedly, a severely localized increase in temperature was seen in the necked region of both specimens, while outside the neck, a temperature increase of 70 °C to 80 °C was calculated.

Using FEM analyses, the average temperature and strain values over the whole gage length of the two samples were obtained and compared with the experimentally recorded data (Figure 18). Beyond certain values of strain, the experimental curves exceed the temperature values calculated by the FEM. This can be related to the heat released due to strain-induced martensitic transformation, which is an exothermic reaction in the investigated steel.[75]

Hence, for the correct calculation of the temperature rise through Eq. [4], the enthalpy of this reaction (ΔH_r) should also be considered. In other words, in the case of metastable microstructures such as those studied in the present work, energy conservation for the adiabatic deformation of the material can be written as follows:

$$Q = \beta W + \Delta H_r = \beta' W, \qquad [5]$$

where the coefficient β' is as follows:

$$\beta' = \beta + \frac{\Delta H_r}{W}. \qquad [6]$$

Thus, to consider the influence of martensitic transformation, β' can be substituted for β in Eq. [4]. In the present work, the experimentally measured temperature increase (ΔT) was used along with the plastic work per unit volume ($\int \sigma d\varepsilon$) of the gage zone (calculated by the FEM) to obtain β' *via* Eq. [4]. The result is presented in Figure 19.

In stable microstructures, less than 10 pct of mechanical energy is restored as metallurgical defects in the material, and the remaining energy arises as thermal energy so that β takes values of 0.9 to 1. However, for the present investigation, with increased deformation, excess heat is released due to phase transformation, and hence, the coefficient β' increases to values higher than unity. This increase in *c*' for the microstructure of the specimen subjected to DRA is sharp at a true strain of ~ 0.1. However, the β' of the CG microstructure shows a gradual increase, which is in agreement with the high and definitely more stable strain hardening of this microstructure, as shown previously in Figure 7(b). The

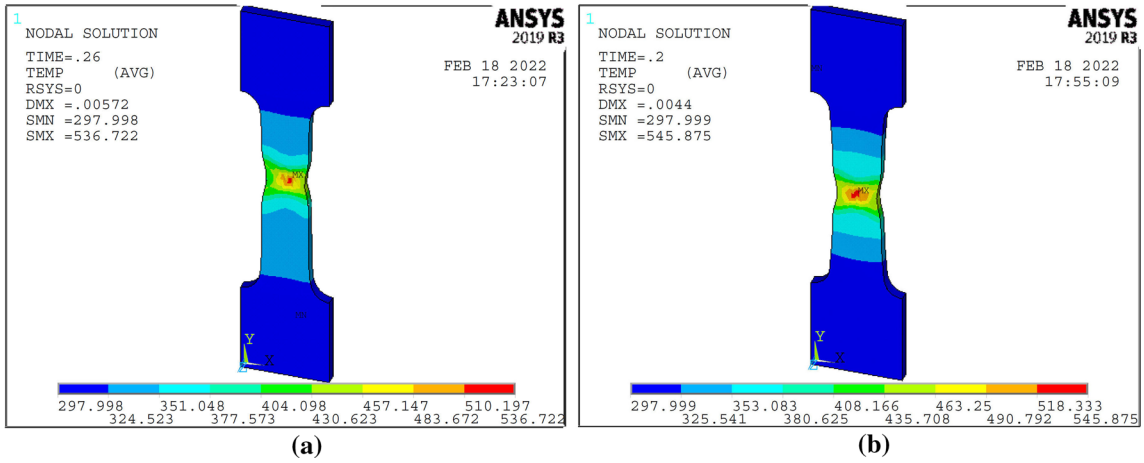

Fig. 17—Temperature contours obtained at the failure strain in high-strain rate tensile testing of the (*a*) CG 301LN and (*b*) DRA T800-1 structures.

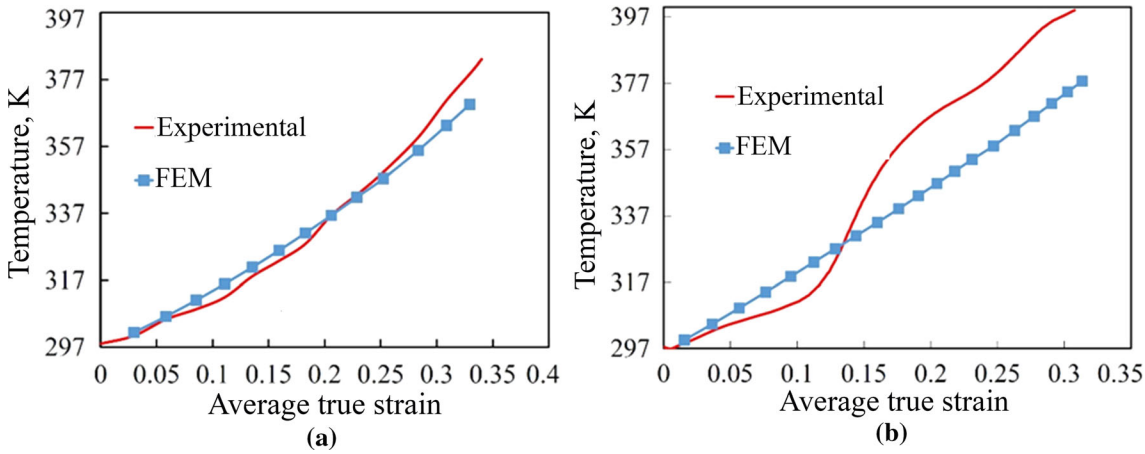

Fig. 18—Average temperatures calculated by the FEM over the whole gage length of the tensile specimens as well as the experimental temperature data recorded for (*a*) CG 301LN and (*b*) DRA T800-1.

sudden release of heat and temperature increases that occurs in the specimen subjected to DRA increases the SFE and stabilize austenite.[76] This may be more pronounced in the center part of the specimen, which undergoes flow localization.

B. *Erichsen Cupping Tests*

1. *Deformation profile*

The distribution of Von Mises strain at the end of the Erichsen tests conducted on both the CG specimen and the specimens subjected to DRA at a high speed equivalent to the true strain rate of 1.5 s^{-1} is presented in Figure 20. A steep strain gradient is obvious in both specimens.

2. *Temperature rise*

The temperature contours obtained at failure in high-speed Erichsen tests are presented in Figure 21.

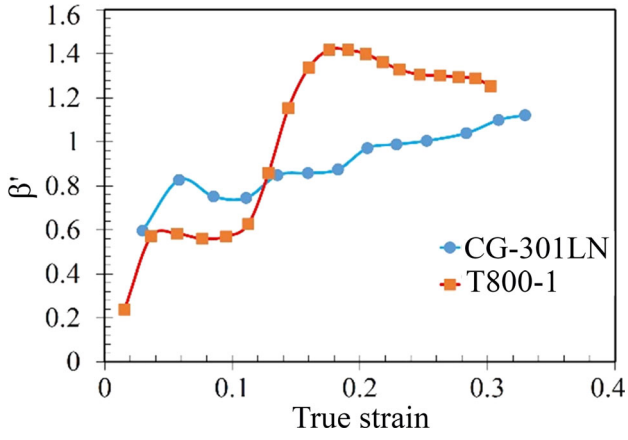

Fig. 19—Variation in the β' coefficient with true strain for the high-speed deformation (strain rate of 1.5 s^{-1}) of CG and DRA T800-1 microstructures.

Maximum values of ~ 150 and 170 °C are predicted for the temperature rise at the end of the Erichsen tests performed on the CG specimen and specimens subjected to DRA, respectively. Note that these high-temperature values are highly localized at the center of the cup and may be reached only if the material withstands the corresponding localized strain. Furthermore, the influence of martensitic transformation is not considered in FEM analyses.

To consider the influence of phase transformation on the temperature rise of the specimens, the coefficient β', which was previously calculated as a function of true strain, and the profiles of plastic work per unit volume calculated by FEM analyses ($\int \sigma d\varepsilon$) are inserted into Eq. 4. The temperature profiles obtained with various average true strains are plotted in Figure 22. The calculated temperatures are slightly higher than those observed in the contours of Figure 21, which is due to the influence of the exothermic phase transformation. Furthermore, the difference between the average strains of 0.2 and 0.1 in the specimen subjected to DRA is much higher than that seen for its CG counterpart. This can be explained by the severe and sharp increase in the β' coefficient for the DRA T800-1 specimen, as previously discussed and shown in Figure 19.

V. DISCUSSION

The present work demonstrates the significant effect of DRA processing on the microstructures of metastable austenitic 301 LN. While SRA produced a fine-grain structure with an average grain size ~ 2.5 μm (Figure 2), ultrafine-grained structures with average grain sizes of 0.53 and 0.75 were exhibited by the DRA T800-1 and DRA T900-1 structures, respectively (see Figures 4 and 5). The microstructures developed by DRA processing exhibited significantly improved tensile properties, as shown in Figure 7. Moreover, tensile straining of the DRA structures at high speed (1.5 s^{-1}) resulted in an extensive deformation-induced martensitic transformation, which varied depending on the grain structure achieved by DRA, as illustrated in Figure 8. Grain size has a significant effect on protecting metastable austenite from martensitic transformation during deformation.[77] Naghizadeh and Mirzadeh[78] reported that the maximum strain hardening in various reverted grain structures of AISI 304 stainless steel is related to the TRIP effect, which is strongly enhanced by increasing grain size due to the increased susceptibility of coarse grains to undergo deformation-induced martensitic transformation. However, the relationship between the martensitic transformation and the grain size exhibited the opposite trend in specimens subjected to DRA.

TEM was applied to obtain insight into the austenitic structures achieved with DRA to characterize the fine features. Upon fast heating at T750-0.1, fast reversion to austenite grains associated with the density of dislocations is promoted, as shown in Figure 23(a). Interestingly, nano-austenite grains reverted from martensite grains are visible in Figure 23(b). However, DRA T800-1 shows two types of reverted γ-grains, grains containing dislocations, marked by yellow ovals, and grains free of dislocations, as shown in Figure 23(c). By increasing the DRA temperature to T900-1, a UFG microstructure of reverted austenite grains was promoted, as illustrated in Figure 23(d). A striking feature of the structure achieved at T900-1 is extensive dislocation recovery, which leads to reverted dislocation-free grains.

It is well known that the strain-induced martensitic transformation process occurs through two main stages during deformation: nucleation and growth. Grain boundaries are favorable sites for the nucleation of α'-martensite during deformation. With decreasing DRA temperature and time, *e.g.*, T750-0.1, the processed microstructure exhibited the finest grain structure, which achieved more grain boundary sites for strain-induced martensite formation. The growth stage mainly depends on the strain rate. In deformation at a high strain rate of 1.5 s^{-1}, the growth stage of the martensitic transformation is limited. Pun *et al.*[79] studied the dependence of strain-induced martensite nucleation and growth in 301LN on the strain rate. They

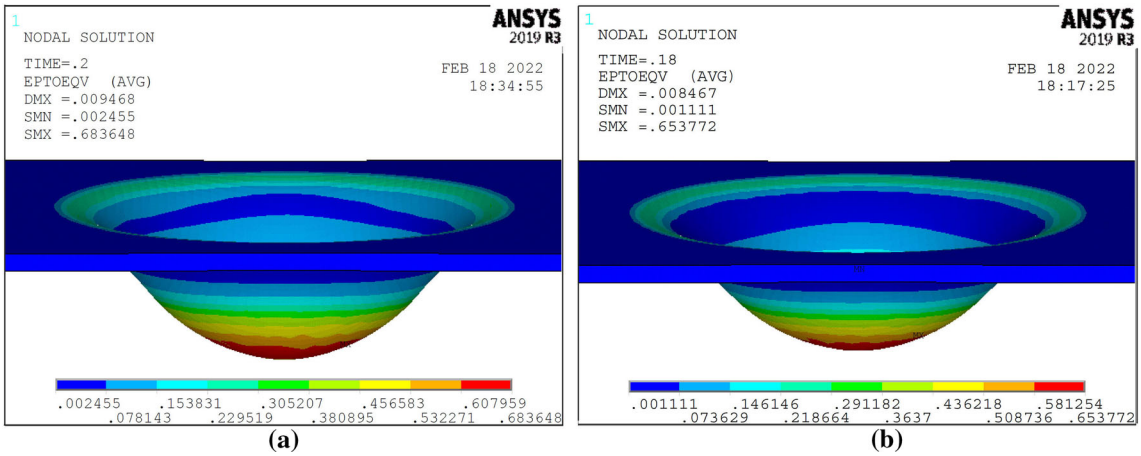

Fig. 20—Contours of the Von Mises equivalent strains at the end of high-speed Erichsen tests: (*a*) CG 301LN and (*b*) DRA-T800-1 structures.

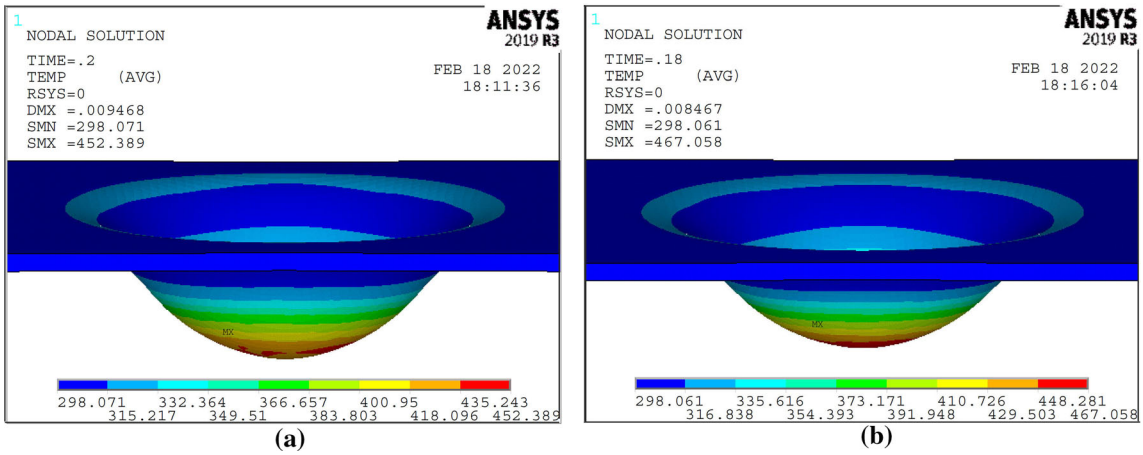

Fig. 21—Temperature contours obtained at the end of high-speed Erichsen tests performed on the (*a*) CG 301LN and (*b*) DRA-T800-1 structures.

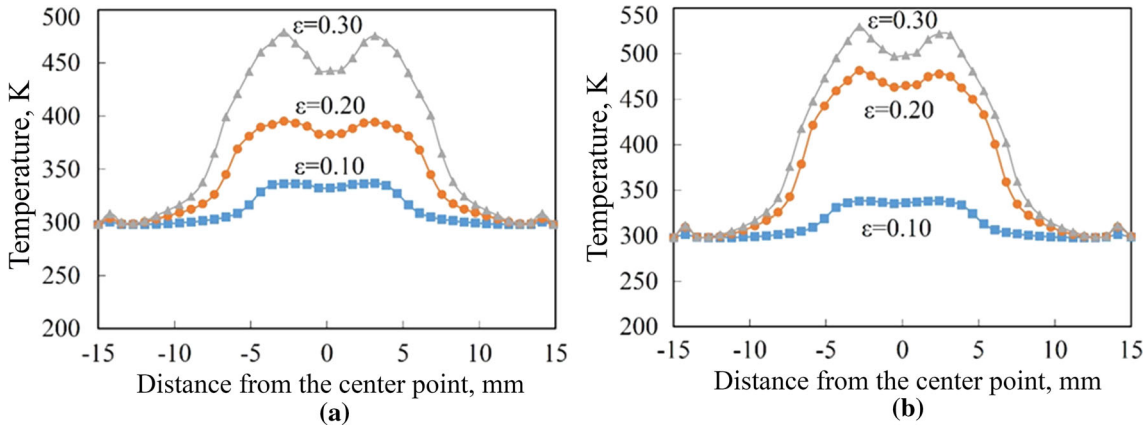

Fig. 22—Temperature profiles obtained at different average true strain values for high-speed Erichsen testing on (*a*) CG 301LN and (*b*) DRA T800-1.

found that at a high strain rate of 0.5 s^{-1}, the growth stage of martensite is minimal. In other words, the nucleation stage of the martensitic transformation is predominant in high-strain rate deformation.

Thus, the martensite fraction decreases with increasing grain size. Moreover, the dislocation density provides more nucleation sites for the new strain-induced martensite. The structure resulting from DRA at T750-0.1 has a higher dislocation density, as shown by the TEM observations in Figure 23. Therefore, during tensile straining at a high strain rate of 1.5 s^{-1}, a higher dislocation density is induced in the structure resulting from DRA; hence, more strain energy accumulates, leading to an increase in the transformation of austenite to martensite.[80]

Although DRA T750-0.1 and T800-1 exhibited higher martensite contents, as shown in Figure 8, their SHRs were lower than the SHR of DRA 900-1 (see Figure 7(b)). In agreement, Somani *et al.*[26] found that the ultrafine reverted submicron grain structure of 301LN revealed a lower strain-hardening rate than the coarse structure. SHR is related to martensite growth and coalescence during deformation.

VI. CONCLUSIONS

The effect of grain refinement by the double reversion treatment on the tensile properties and stretch formability of metastable austenitic 301LN steel in high-speed deformation (1.5 s^{-1}, 50 mm s^{-1}) was investigated. Adiabatic heating, temperature, and strain analyses were performed by a FEM on the DRA structures subjected to the high-speed Erichsen cupping tests. The most important results of the present study are briefly summarized as follows:

1. The tensile properties of the structures resulting from DRA in high-speed tensile testing with a strain rate of 1.5 s^{-1} are markedly higher than those of their CG 301LN counterpart. A high combination of yield strength (~ 950 MPa), tensile strength (1050

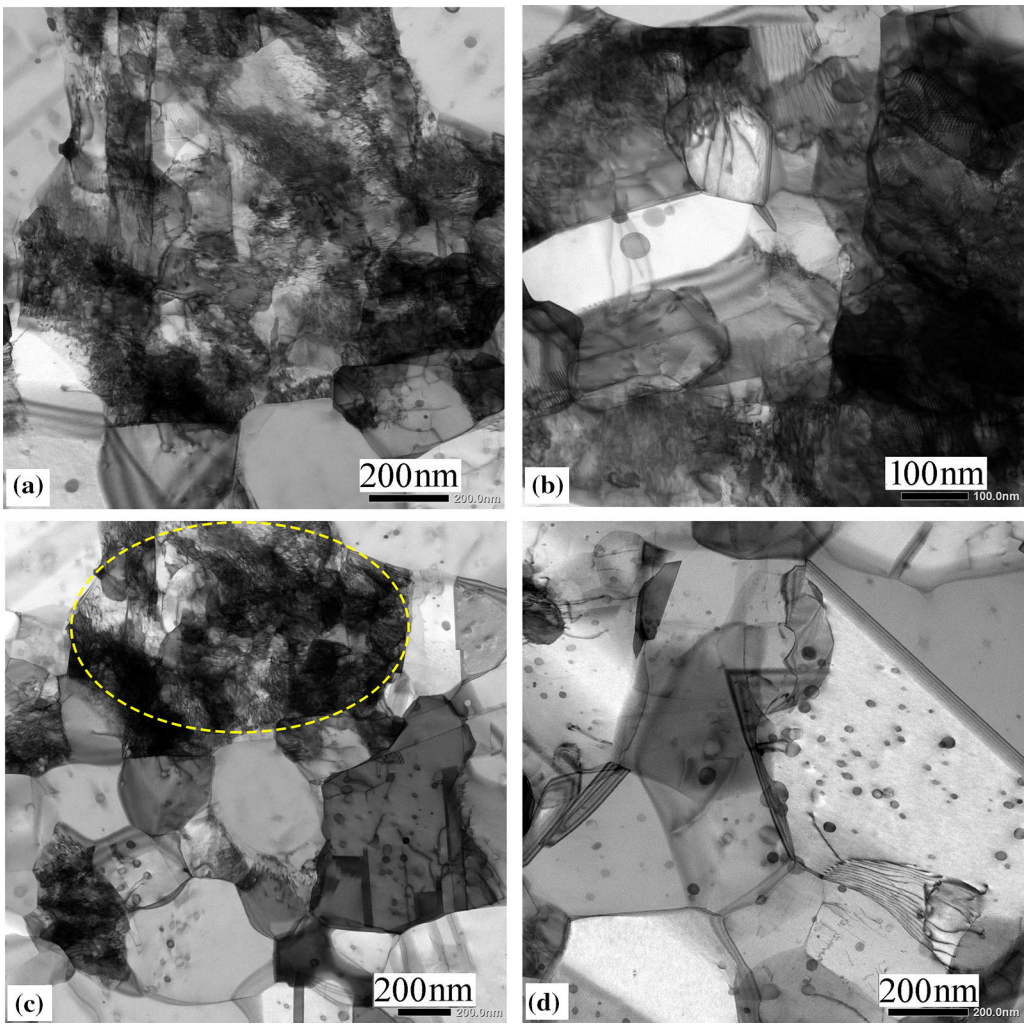

Fig. 23—TEM micrographs showing representative DRA structures of 301LN processed at (*a*) T750-1, (*c*) T800-1, and (*d*) T900-1; (*b*) the high-magnification image of DRA T750-1.

MPa), and ductility (35 pct) is obtained after DRA at 800 °C for 1 second.
2. The formability performance, represented by the EI, of the structures resulting from DRA during testing at a high punching speed of 50 mm s^{-1} is comparable to that at a low speed.
3. Due to grain refinement, DRA T800-1 exhibits a 125 pct higher mechanical strength and a 15 pct lower EI than its CG structure counterpart.
4. The surface roughness of the stretched samples decreased due to the grain-refined structures achieved *via* the DRA process.
5. A comparison of the temperature profiles calculated by the FEM simulation of the tensile tests with those obtained in experiments showed the influence of the martensitic exothermic reaction on the temperature rise of the deformed specimens. As a result, values higher than unity were reached for the modified Taylor–Quinney parameter. The effect was more pronounced in the material subjected to DRA, where martensite formation led to temperature increases of ~ 15 pct in the center of the Erichsen cupped specimen.

ACKNOWLEDGMENT

The authors express their gratitude to the Interreg Nord Program and the Regional Council of Lapland for funding this research through the InTeMP project, No. NYPS 20202486.

CONFLICT OF INTERESTS

The authors declare that they have no known competing financial interests or personal relationships that could have appeared to influence the work reported in this paper.

FUNDING

Open Access funding provided by University of Oulu including Oulu University Hospital.

REFERENCES

1. Z. Xiong, I. Timokhina, and E. Pereloma: Progress. *Mater. Sci.*, 2021, vol. 118, p. 100764.
2. The Materials Information Society: *ASM Specialty Handbook: Stainless Steel*, ASM Int., Metals Park, OH, 1994, p. 314.
3. J. Talonen and H. Hanninen: *Acta Mater.*, 2007, vol. 55, pp. 6108–18.
4. R.D.K. Misra, Z. Zhang, P.K.C. Venkatasurya, M.C. Somani, and L.P. Karjalainen: *Mater. Sci. Eng. A.*, 2010, vol. 527, pp. 7779–92.
5. R.D.K. Misra, Z. Zhang, P.K.C. Venkatasurya, M.C. Somani, and L.P. Karjalainen: *Mater. Sci. Eng. A.*, 2011, vol. 528, pp. 1889–96.
6. M. Isakov, M. May, S. Hiermaier, and V.T. Kuokkala: *Mater. Des.*, 2016, vol. 106, pp. 258–72.
7. N.I. Vazquez-Fernandez, T. Nyyssonen, M. Isakov, M. Hokka, and V.T. Kuokkala: *Acta Mater.*, 2019, vol. 176, pp. 134–44.
8. A. Järvenpää, M. Jaskari, A. Kisko, and P. Karjalainen: *Metals.*, 2020, vol. 10, p. 281.
9. J. Liu, X.T. Deng, L. Huang, Z.D. Wang, and R.D.K. Misra: *Steel Res. Int.*, 2018, vol. 89, p. 1700496.
10. C. Lei, X. Li, X. Deng, Z. Wang, and G. Wang: *Mater. Sci. Eng. A.*, 2018, vol. 709, pp. 72–81.
11. R.D.K. Misra, X.L. Wan, V.S.A. Challa, M.C. Somani, and L.E. Murr: *Mater. Sci. Eng. A.*, 2015, vol. 626, pp. 41–50.
12. A.S. Hamada, A.P. Kisko, P. Sahu, and L.P. Karjalainen: *Mater. Sci. Eng. A.*, 2015, vol. 628, pp. 154–59.
13. A. Kisko, A.S. Hamada, J. Talonen, D. Porter, and L.P. Karjalainen: *Mater. Sci. Eng. A.*, 2016, vol. 657, pp. 359–70.
14. V.S.A. Challa, R.D.K. Misra, M.C. Somani, and Z.D. Wang: *Mater. Sci. Eng. A.*, 2016, vol. 661, pp. 51–60.
15. D.M. Xu, G.Q. Li, X.L. Wan, R.D.K. Misra, X.G. Zhang, G. Xu, and K.M. Wu: *Mater. Sci. Eng. A.*, 2018, vol. 720, pp. 36–48.
16. M. Naghizadeh and H. Mirzadeh: *Metall. Mater. Trans. A.*, 2016, vol. 47A, pp. 4210–16.
17. M. Moallemi, A. Najafizadeh, A. Kermanpur, and A. Rezaee: *Mater. Sci. Eng. A.*, 2011, vol. 530, pp. 378–81.
18. A. Abdi, H. Mirzadeh, M.J. Sohrabi, and M. Naghizadeh: *Metall. Mater. Trans. A.*, 2020, vol. 51A, pp. 1955–59.
19. D. Chatterjee: *Mater. Today: Proc.*, 2021, vol. 46, pp. 10604–11.
20. G.P. Dinda, H. Rosner, and G. Wilde: *Scripta Mater.*, 2005, vol. 52, pp. 577–82.
21. H. Zhang, W. Cheng, J. Fan, B. Xu, and H. Dong: *Mater. Sci. Eng. A.*, 2015, vol. 637, pp. 243–50.
22. S. Hwang, M. Park, Y. Bai, A. Shibata, W. Mao, H. Adachi, M. Sato, and N. Tsuji: *Acta Mater.*, 2021, vol. 205, p. 116543.
23. D.M. Field and D.C. Van Aken: *Metall. Mater. Trans. A.*, 2016, vol. 47A, pp. 1912–17.
24. K. Al-Fadhalah and M. Aleem: *Metall. Mater. Trans. A.*, 2018, vol. 49A, pp. 1121–39.
25. M.J. Sohrabi, M. Naghizadeh, and H. Mirzadeh: *Arch. Civ. Mech. Eng.*, 2020, vol. 20, p. 124.
26. M.C. Somani, M. Jaskari, S. Sadeghpour, C. Hu, R.D.K. Misra, T. Tunnyo, C. Yang, and L.P. Karjalainen: *Mater. Sci. Eng. A.*, 2020, vol. 793, p. 139885.
27. C.Y. Hu, M.C. Somani, R.D. Misra, and C.G. Yang: *J. Mech. Behav. Biomed. Mater.*, 2020, vol. 104, p. 103666.
28. M.C. Somani, P. Juntunen, L.P. Karjalainen, R.D.K. Misra, and A. Kyrolainen: *Metall. Mater. Trans. A.*, 2009, vol. 40A, pp. 729–44.
29. A. Järvenpää, M. Jaskari, J. Man, and L.P. Karjalainen: *Mater. Sci. Eng. A.*, 2017, vol. 703, pp. 280–92.
30. A. Järvenpää, M. Jaskari, J. Man, and L.P. Karjalainen: *Mater. Charac.*, 2017, vol. 127, pp. 12–26.
31. A. Järvenpää, M. Jaskari, J. Man, and L.P. Karjalainen: *Metals.*, 2018, vol. 8, p. 109.
32. A. Järvenpää, L.P. Karjalainen, and M. Jaskari: *Int. J. Fatigue.*, 2014, vol. 65, pp. 93–98.
33. A.S. Hamada, L.P. Karjalainen, P.K.C. Venkata Surya, and R.D.K. Misra: *Mater. Sci. Eng. A.*, 2011, vol. 528, pp. 3890–96.
34. A.S. Hamada: *Metall. Mater. Trans. A.*, 2013, vol. 44A, pp. 1626–30.
35. J. Liu, X.T. Deng, L. Huang, and Z.D. Wang: *Tribol. Int.*, 2020, vol. 152, p. 106520.
36. H. Zhang, P. Xue, L.H. Wu, Q.N. Song, D. Wang, B.L. Xiao, and Z.Y. Ma: *Corro. Sci.*, 2020, vol. 174, p. 108847.
37. A.S. Hamada, L.P. Karjalainen, and M.C. Somani: *Mater. Sci. Eng. A.*, 2006, vol. 431, pp. 211–17.
38. N. Gong, C. Hu, B. Hu, B. An, and R.D.K. Misra: *J. Mech. Behav. Biomed. Mater.*, 2020, vol. 101, p. 103433.
39. K.C. Nune, M.C. Somani, C.T. Spencer, and R.D.K. Misra: *Mater. Technol.*, 2017, vol. 32, pp. 22–31.
40. A.S. Hamada, A. Järvenpää, E. Ahmed, P. Sahu, and A.I.Z. Farahat: *Mater. Des.*, 2016, vol. 94, pp. 345–52.
41. M. Droste, A. Järvenpää, M. Jaskari, M. Motylenko, A. Weidner, P. Karjalainen, and H. Biermann: *Fatigue Fract. Eng. Mater. Struct.*, 2021, vol. 44, pp. 43–62.
42. A. Järvenpää, M. Jaskari, M. Keskitalo, K. Mäntyjärvi, and P. Karjalainen: *AIP Conf. Proc.*, 2019, vol. 2113, p. 160008.
43. A. Järvenpää, S. Ghosh, A. Khosravifard, M. Jaskari, and A. Hamada: *Mater. Sci. Eng. A.*, 2021, vol. 808, p. 140917.
44. M. Linnemann, V. Psyk, E. Djakow, R. Springer, W. Homberg, and D. Landgrebe: *Procedia. Manuf.*, 2019, vol. 27, pp. 21–26.
45. T. Trzepieciński: *Metals.*, 2020, vol. 10, p. 779.
46. T. Ungar: *Scripta Mater.*, 2004, vol. 51, pp. 777–81.
47. T. Shintani and Y. Murata: *Acta Mater.*, 2011, vol. 59, pp. 4314–22.
48. S.G. Chowdhury, S. Das, and P. De: *Acta Mater.*, 2005, vol. 53, pp. 3951–59.
49. M. Ashiq, P. Dhekne, A. Hamada, P. Sahu, B. Mahato, R.K. Minz, S.G. Chowdhury, and L.P. Karjalainen: *Metall. Mater. Trans. A.*, 2017, vol. 48A, pp. 4842–56.
50. H. Kamali, H. Xie, H. Bi, E. Chang, H. Xu, H. Yu, and Z. Jiang: *Mater. Sci. Eng. A.*, 2021, vol. 804, p. 140724.
51. A.H. Cottrell and B.A. Bilby: *Proc. Phys. Soc. A.*, 1949, vol. 62, pp. 49–62.
52. R. Song, D. Ponge, D. Raabe, J.G. Speer, and D.K. Matlock: *Mater. Sci. Eng. A.*, 2006, vol. 441, pp. 1–17.
53. Y. Ma, B. Sun, A. Schökel, W. Song, D. Ponge, D. Raabe, and W. Bleck: *Acta Mater.*, 2020, vol. 200, pp. 389–403.
54. A. Mandal, S. Morankar, M. Sen, S. Samanta, S.B. Singh, and D. Chakrabarti: *Metall. Mater. Trans. A.*, 2020, vol. 51A, pp. 3886–905.
55. M. Saeglitz and G. Krauss: *Metall. Mater. Trans. A.*, 1997, vol. 28A, pp. 377–87.
56. S. Yan, T. Liang, Z. Wang, B. Yan, T. Li, and X. Liu: *Mater. Sci. Eng. A.*, 2020, vol. 773, p. 138732.

57. A. Weidner, K. Fischer, and H. Biermann: *Mater. Sci. Eng. A.*, 2021, vol. 799, p. 140197.
58. M. Aydin, X. Wu, K. Cetinkaya, M. Yasar, and I. Kadi: *Eng. Sci. Technol. Int. J.*, 2018, vol. 21, pp. 760–68.
59. N. Kamikawa and H. Morino: *Metall. Mater. Trans. A.*, 2019, vol. 50A, pp. 5023–37.
60. O. Saray, G. Purcek, I. Karaman, and H.J. Maier: *Metall. Mater. Trans. A.*, 2013, vol. 44A, pp. 4194–206.
61. D.M. Sekban, O. Saray, S.M. Aktarer, G. Purcek, and Z.Y. Ma: *Mater. Sci. Eng. A.*, 2015, vol. 642, pp. 57–64.
62. G. Scavino, F. D'aiuto, P. Matteis, P. Russo Spena, and D. Firrao: *Metall. Mater. Trans. A.*, 2010, vol. 41A, pp. 1493–501.
63. G. Fargas, A. Zapata, J.J. Roa, I. Sapezanskaia, and A. Mateo: *Metall. Mater. Trans. A.*, 2015, vol. 46A, pp. 5697–707.
64. A.S. Hamada, A. Kisko, A. Khosravifard, M.A. Hassan, L.P. Karjalainen, and D. Porter: *Mater. Sci. Eng. A.*, 2018, vol. 712, pp. 255–65.
65. P. Gibson and U. Holzwarth: *Nat. Nanotechnol.*, 2011, vol. 6, p. 534.
66. R.A. Renzetti, H.R.Z. Sandim, R.E. Bolmaro, P.A. Suzuki, and A. Möslang: *Mater. Sci. Eng. A.*, 2012, vol. 534, pp. 142–46.
67. R. Kishor, L. Sahu, K. Dutta, and A.K. Mondal: *Mater. Sci. Eng. A.*, 2014, vol. 598, pp. 299–303.
68. M.E. Tahawy, Y. Huang, T. Um, H. Choe, J.L. Lábár, T.G. Langdon, and J. Gubicza: *J. Mater. Res. Technol.*, 2017, vol. 6, pp. 339–47.
69. S. Ghosh, A.K. Singh, and S. Mula: *Mater. Des.*, 2016, vol. 100, pp. 47–57.
70. H.K. Yeddu, V.I. Razumovskiy, A. Borgenstam, P.A. Korzhavyi, A.V. Ruban, and J. Agren: *Acta Mater.*, 2012, vol. 60, pp. 6508–17.
71. H.K. Yeddu, T. Lookman, and A. Saxena: *J. Mater. Sci.*, 2014, vol. 49, pp. 3642–51.
72. R.D.K. Misra, B. Ravi Kumar, M. Somani, and P. Karjalainen: *Scripta Mater.*, 2008, vol. 59, pp. 79–82.
73. R. Becker: *Acta Mater.*, 1998, vol. 46, pp. 1385–401.
74. L. Cho, P.E. Bradley, D.S. Lauria, M.L. Martin, M.J. Connolly, J.T. Benzing, E.J. Seo, K.O. Findley, J.G. Speer, and A.J. Slifka: *Acta Mater.*, 2021, vol. 206, p. 116635.
75. N.I. Vazquez Fernandez, G.C. Soares, J.L. Smith, J.D. Seidt, M. Isakov, A. Gilat, and V.T. Kuokkala: *J. Dyn. Behav. Mater.*, 2019, vol. 5, pp. 221–29.
76. P. Xia, F.J.C. Rodríguez, and I. Sabirov: *Mater. Sci. Eng. A.*, 2020, vol. 793, p. 139829.
77. R.N. Dehsorkhi, S. Sabooni, F. Karimzadeh, A. Rezaeian, and M.H. Enayati: *Mater. Des.*, 2014, vol. 64, pp. 56–62.
78. M. Naghizadeh and H. Mirzadeh: *Steel Res. Int.*, 2019, vol. 90, p. 1900153.
79. L. Pun, G.C. Soares, M. Isakov, and M. Hokka: *Mater. Sci. Eng. A.*, 2022, vol. 831, p. 142218.
80. H. Dong, Z.C. Li, M.C. Somani, and R.D.K. Misra: *J. Mech. Behav. Biomed. Mater.*, 2021, vol. 119, p. 104489.